Modelling of interactions between lipid bilayers and nanoparticles of various degrees of hydrophobicity

Dissertation

zur Erlangung des akademischen Grades
Doctor rerum naturalium
(Dr. rer. nat.)

vorgelegt der

Fakultät für Mathematik und Naturwissenschaften der Technischen Universität Dresden

von

Chanfei Su

geboren am 08. Marz 1989 in Fujian, China

Defense date: 16_{th} October, 2018
Gutachter: Prof. Dr. Jens-Uwe Sommer
Dr. Fabrice Thalmann

Acknowledgments

At first, I would like to thank my supervisor Prof. Dr. Jens-Uwe Sommer. Throughout this project, he has been supporting and mentoring, while providing insightful discussions, knowledge, patience and a great working environment.

I also gratefully thank my colleagues past and present including Prof. Dr. Holger Merlitz, Dr. Hauke Rabbel, Dr. Marco Werner, Markus Koch, Dr. Olivier Benzerara in Institute Charles Sadron, Strasbourg and AnnaSofia Tascini in Imperial College London, UK, who provided knowledge and valuable discussions that are beneficial to this work. I further thank co-supervisor within the SNAL network, Dr. Fabrice Thalmann, who gave me a lot of support and hosted me during the secondment in Strasbourg. Special thanks also belong to the secretary in the institute of theoretical physics (ITP), Ms. Nicole Krause, who is always kind and arranged many things. I also thank the SNAL initial training network for financial support and scientific trainings within the network, the Leibniz institute of polymer research for the technique support and ZIH at the Technical University of Dresden for computer resources. And I appreciate the opportunity to be trained in this research group and within the SNAL network.

Last, but not least, I would like to thank my family and friends for encouraging and supporting me during this scientific journey, especially May and Toby in Dresden for their warm company.

All these people have been essential to the completion of my thesis. And for that, I am extremely grateful.

Abstract

Biological membranes are mainly composed of two layers of lipids, various kinds of proteins and organic macromolecules, forming the protective barriers that separate the inner milieu of living cells from the environment. The possibility of penetrating the membrane is of great importance for biomedical applications. Recently, a lot of attention has been given to the mechanisms and the details of the interactions between the membrane and nanoparticles, as well as to the development of effective delivery strategies. A manipulation of the hydrophobicity of nanoparticles can facilitate the translocation through the membrane. Modifying the physical/chemical properties of the membrane through oxidation can also influence the delivery of nanoparticles or macromolecules into the cell.

In this work, using coarse-grained molecular dynamics simulations, the passive translocation of nanoparticles with a size of about 1 nm and with tunable degrees of hydrophobicity through lipid membranes is studied. It is shown that a window of nanoparticle translocation with a sharp maximum is located at a certain hydrophobicity in between fully hydrophilic and fully hydrophobic characters. By combining direct simulations with umbrella sampling simulations, the free energy landscapes for nanoparticles covering a wide range of hydrophobicities are obtained. The directly observed translocation rate of the nanoparticles can be mapped to the mean escape rate through the calculated free energy landscapes, and the maximum of translocation can be related with the maximally flat free energy landscape. For nanoparticles with the balanced hydrophobicity, the bilayer forms a remaining barrier of a few k_BT and can be spontaneously surmounted. Further investigations are conducted to explore the cooperative effects of a larger number of nanoparticles and their impact on membrane properties such as membrane permeability for solvent, the area per lipid, and the orientation order of lipid tails. By calculating the partition of nanoparticles between water and oil phases, the microscopic parameter, *i.e.* the hydrophobicity of nanoparticles, can be mapped to an experimentally accessible partition coefficient. The studies reveal a generic mechanism for spherical nanoparticles to overcome biological membrane-barriers without the need of biologically activated processes.

Two oxidatively modified lipids are studied on coarse-grained level using molecular dynamics simulations. The findings support the view that lipid oxidation leads to a change of the lipid conformation: lipid tails tend to bend toward the lipid head-tail interface due to the presence of hydrophilic oxidized beads. This change in conformation can further influence structural properties, elasticity and membrane permeability: an increase of the area per

lipid, accompanied with decrease of the membrane thickness and order parameter of the lipid tails; a sharp drop of stretching modulus; a significant increase of the membrane permeability for water.

Oxidized lipid bilayers interacting with NPs of various degrees of hydrophobicity are further studied. The critical hydrophobicity corresponding to the maximum translocation rate of NPs, shifts towards the hydrophilic region, which coincides with the same decrease in percentage of the average hydrophobicity in the core of the membrane upon oxidation. Around the critical point of NPs' hydrophobicity, a significant increase of the translocation rate of NPs through the oxidized bilayers is observed, when compared to non-oxidized bilayers. This is associated with a deterioration of the free energy barrier for NPs inside the oxidized bilayers, resulting from oxidation effects. These findings are consistent with the studies of the mean escape rate through the free energy landscapes using Kramers theory. Regarding the membrane perturbation induced by NPs of various hydrophobicity, the data obtained with oxidized lipid bilayers present the same general trend as in the case of the non-oxidized lipid bilayer. These findings provide a better understanding of the interaction between NPs and oxidized lipid bilayers, and open a possibility to facilitate drug delivery.

Contents

1 Introduction 1

1.1 Lipid Bilayers 1
1.2 Oxidized Lipid Bilayers 2
1.3 Experimental Methodology 4
1.4 Lipid Models 5
1.5 The Lipid Bilayer Interacting with NPs 6
1.6 Thesis Overview 7

2 State of the art 9

2.1 Molecular Dynamics Simulations of Lipid Bilayers 9
2.1.1 Equations of Motion and the Integrations of Equations of Motion 10
2.1.2 Interaction Potentials 12
2.1.3 Periodic Boundary Conditions 14
2.1.4 Barostats and Thermostats 15
2.2 Umbrella Sampling Simulation 19
2.2.1 The Basics of Umbrella Sampling Method 20
2.2.2 Analyzing Umbrella Sampling Results by WHAM 23
2.2.3 The Principle of Choosing Bias Potential 24

3 Lipid Membranes interacting with Nanoparticles of Various Degrees of Hydrophobicity 25

3.1 Introduction 25
3.2 Coarse-grained Model and Simulation Setups 27
3.3 Results and Discussions 31
3.3.1 NPs-membrane Interactions 31
3.3.2 NPs Translocation 33
3.3.3 Concentration Effect of NPs 35
3.3.4 The Effect of Hydrophobicity on Kinetic Pathways 38
3.3.5 Potential of Mean Force 39
3.3.6 Hydrophobicity Scale 41
3.3.7 Solvent Permeation and Membrane Perturbation Induced by NPs 45
3.4 Summary 47

4 Coarse-grained Model of Oxidized Lipids and their Interactions with NPs of Varying Hydrophobicities 51

4.1 Introduction 51
4.2 Coarse-grained Model and Simulation Details 52
4.3 Results and Discussions 54
4.3.1 Characterizing the Oxidized Lipid Membranes 54
4.3.2 Oxidized Lipid Membranes Interacting with NPs of Various Degrees of Hydrophobicity 59
4.4 Summary 65

5 Summary and Outlook 69

1 Introduction

1.1 Lipid Bilayers

Lipid bilayers are the main components of cell membranes in living materials. They act as protective barriers, which separate the contents of living cells from the environment but allow for exchange of substances and informations between them. From skin protection [1, 2] to drug delivery [3,4], lipid membranes play important roles in life. Moreover, lipid bilayers get involved in many cellular activities and metabolic activities, *e.g.* endocytosis and exocytosis [5,6]. Many interesting topics of lipid bilayers have been studied such as their interactions with nanoparticles (NPs) and small molecules (especially the relative translocation process), lipid phase transitions in the membrane, oxidized lipid membranes, biological membranes containing the mixture of lipids, proteins and deoxyribonucleic acid (DNA).

Biological membranes mainly consist of various lipids, organic macromolecules and proteins. Cell membranes are often composed of three main types of lipids, *i.e.* phospholipids, cholesterol and glycolipids. To understand the general physical properties of the lipid membrane, it is common to use simplified lipid bilayers that are composed of two layers of amphiphilic phospholipids, instead of real biological membranes. Most studies of the bilayers are focused on the liquid phase, which is biologically relevant. Generally, the phospholipid consists of a hydrophilic head group and a hydrophobic tail group (usually, two fatty acid chains). As a consequence, when immersed into water, lipid heads are exposed and directly contact with water molecules while the lipid tails are shielded by the surrounding of lipid heads, as shown in Figure1.1. Depending on the shapes, lipids group together into different packing arrangements, *e.g.* lipid bilayers, micelles and inverted micelles [7], as sketched in Figure1.2. The first model of biomembrane was first proposed in 1925 [8]. In experiments, a structure of bilayer was observed [8]. A refined model of biomembrane, so-called fluid mosaic model [9], was further proposed in 1972. In the fluid

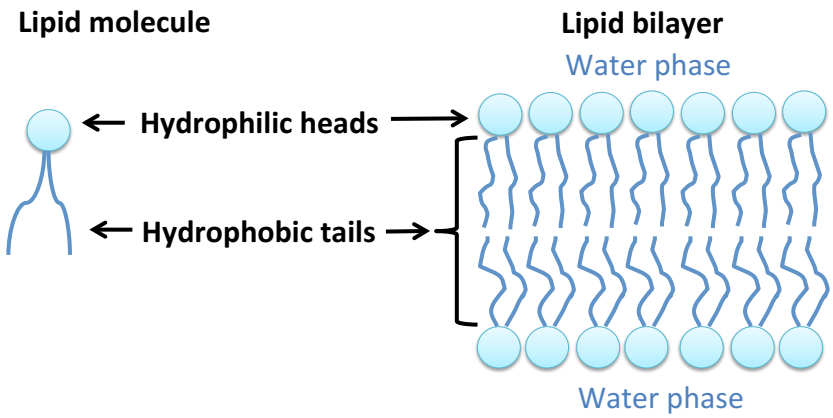

Figure 1.1: Sketch of the lipid (left panel) and assembled lipid bilayer (right panel).

mosaic model, a bilayer was composed of different types of lipids, and proteins attached or embedded in the membrane, as shown in Figure1.3[10].

One of the great challenges in biomembrane sciences is to understand the mechanisms that govern NPs translocation through the lipid bilayer. NPs are typically one of the candidates that are responsible for the drug delivery, gene delivery, therapy and diagnostics. The sizes, shapes, surface charge and hydrophobicity of NPs affect the uptake of NPs. NPs can also be decorated with polymers or functional groups (amino, carboxylic, ligand) to improve drug delivery. Particularly, AuNPs attract a lot of attention due to their biocompatibility, optical properties and surface bonding with ligand. Despite the fact that NPs offer various advantages in the nanomedicine, the concerns about the toxicity of NPs still exist. Therefore, understanding the mechanism of NPs translocation through the membrane and their relevant influence on the membrane is of great importance.

1.2 Oxidized Lipid Bilayers

Biological membranes are essential in the control of nutrients permeating in and leaking out of cells, and execute a variety of cellular processes. Oxidative stress can impact cellular activities and lipid oxidation products can alter the properties of cell membranes such as the mobility of the lipid molecules and membrane permeability. Particularly, unsaturated fatty acids and phospholipids are prone to oxidative modification at the weak carbon-

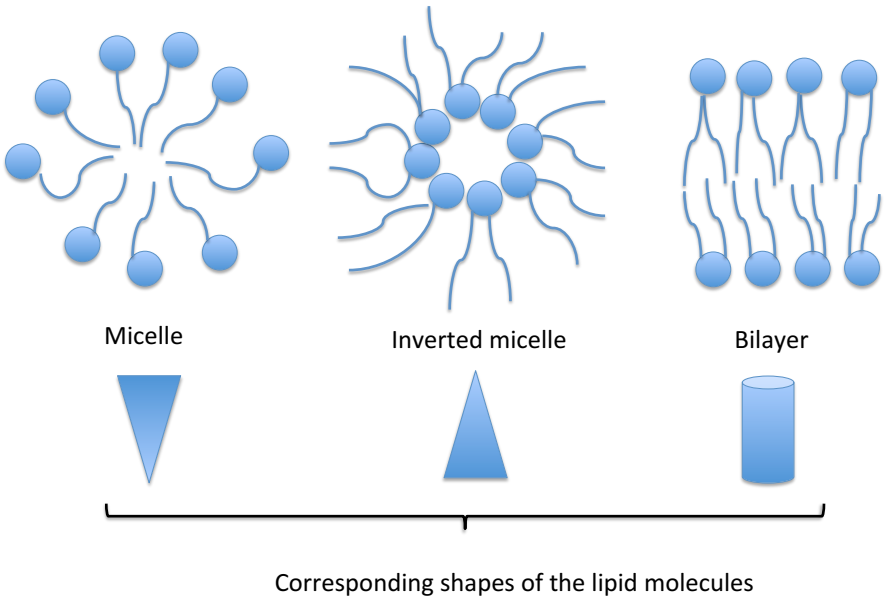

Figure 1.2: Structures of formations assembled by the corresponding lipids with different molecular shapes.

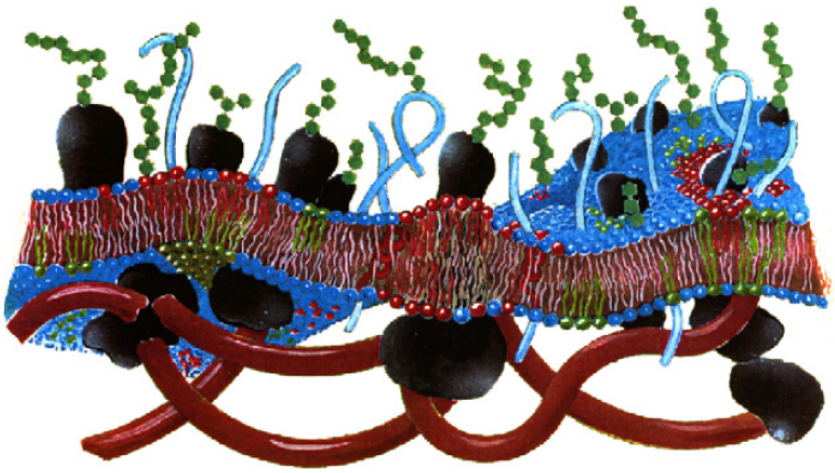

Figure 1.3: Mosaic model of the membrane: lipid bilayers and proteins attached/embedded in the membrane, adopted from Ref. [10].

carbon double bonds. Oxidation reactions lead to changes of the conformation of lipids, thus, alter the structural and dynamical properties of the membrane. The protection of membranes from oxidation stress becomes critical. Recent studies show that the mobility of phospholipids in single unilamellar vesicles is reduced in the lateral diffusion [11]. When oxidized by atmospheric pressure plasma irradiation, the lateral mobility of lipids decreases [12]. Moreover, oxidation of membrane lipids can induce phase separations in the densely packed dipalmitoylphosphatidylcholine (DPPC)-rich membranes [13] and even destroy lipid bilayer packing both in vitro[14] and in vivo[15]. Recent studies show that lipid oxidation products increase membrane permeability for water [16,17], and reduce the barrier when translocating through membrane [18,19]. In addition, oxidation products can influence cellular processes[20], signaling processes [21] and are related with various diseases [22,23], including Parkingson's [24,25], Alzheimer's diseases [26].

1.3 Experimental Methodology

The membrane properties can vary by several factors, *e.g.* types of lipids composing the lipid bilayer, temperature and other molecules such as proteins, cholesterols and alcohols. The properties of the membrane, *e.g.* the order parameter of lipids, the area per lipid, can be measured accurately via experiments or simulations. Therefore, it allows a direct comparison between experimental and simulation results. From a computational point of view, these quantities are highly useful when monitoring the equilibration process. Here, we mention experimental techniques commonly used to observe properties of the membrane.

The density profile of lipid bilayers can be measured by diffraction techniques [27], which can be directly compared with atomistic simulation results and used to parameterize the simulation model. The density profile not only gives the general structure of the lipid bilayer, but also its thickness. Namely, the thickness of the bilayer can be extracted from the distance between two peaks of lipid head groups distribution. Generally, the thickness of the bilayer is inversely proportional to the area per lipid.

The order parameter of lipids is one of the criteria to determine the phase state of lipids, which can be generally measured by Nuclear Magnetic Resonance (NMR) [28] and fluorescence depolarization experiments [29]. When the lipids are arranged parallel to the

z direction, the order parameter of lipid tail is defined as follows:

$$P_2 = \langle 3\cos^2\theta - 1\rangle/2, \tag{1.1}$$

where θ is the angle between the end-to-end vector of the lipid tail and the z-axis. By definition, $P_2 = 0$ denotes random orientation, while $P_2 = 1$ indicates alignment parallel to z-coordinate (normal to the bilayer plane). For example, in the gel phase, lipid chains are arranged in parallel indicating high order parameter of lipids. Vice versa, low value of the order parameter represents disordered lipids in the liquid state.

Another fundamental characteristic of the lipid bilayer is the area per lipid [30], which is directly measured by X-ray, neutron scattering experiments [27] and electron density profile method [31], or derived from order parameter profiles [32].

1.4 Lipid Models

Multiple lipid models have been developed in different length and time scales, which are reviewed in recent papers [10,33,34]. According to the levels of resolution to represent molecules in simulations, models of lipids can be divided into atomistic and coarse-grained (CG). For atomistic force fields such as CHARMM [35] and GROMOS96 [36], each atom in the molecule is represented as an individual bead in the simulation. Atomistic simulations contain a realistic description of the lipids and provide chemical details. Therefore, they are useful to calculate the dynamic properties of the system, such as the diffusion of lipid molecules, the dynamics of hydrogen bonding in the interface, and provide detailed information about how small molecules affect the structure of bilayers. However, due to the representation of the atoms, atomistic simulations are computationally expensive and limited to shorter time and length scales.

To overcome this barrier, one can implement a CG model to construct the lipid bilayer, which generally uses less detailed resolution by mapping a group of atoms into one bead. This representation allows to simulate larger systems on larger time scales and neglects the detailed information about the single lipid molecule that is less important for the study. The most popular CG model for the lipid bilayer is the MARTINI force field [37,38], which is an empirical model adjusted by the atomistic simulation results. It has gained popularity due to its applicability in a wide range. The strategy behind the MARTINI model is

mapping four atoms into one CG bead. In the simple representation, DPPC molecules are presented by 12 CG beads. As a consequence, larger time steps are used compared with atomistic simulations, which allows to simulate the larger lipid bilayer system on longer time scales. Apart from the study of lipid bilayers, the MARTINI model can be extended to study proteins [39], DNA [40] and carbohydrates [41]. Other CG models are even more generic, such as the Cook model and Lenz model. In the representation of the Cook model, the lipid molecule consists of three beads (one hydrophilic head bead and two hydrophobic tail beads). It is implemented to study the relation between the membrane curvature and different shapes of lipids [42]. For the Lenz model [43], the lipid molecule is represented by seven beads. It successfully reproduces the phase behaviors of monolayers [44] and bilayers [45].

Another effective CG model of lipid bilayers is bond fluctuation model (BFM) with explicit solvent [46,47], which is basically a lattice model for Monte Carlo simulations. In the description of BFM, the monomers of lipid molecules are presented as cubes occupying the lattice for the excluded volume effect, and the bond connecting two monomers is constrained to a set of 108 bond vectors. Therefore, a configuration of a lipid molecule is a combination of cubes and a set of corresponding bond vectors. In the BFM, a short range interaction is introduced between hydrophobic and hydrophilic monomers, which is mediated to model the hydrophobicity effect. The moves of monomers are accepted according to the Metropolis algorithm while the configurations of lipid molecules follow the requires of excluded volume and bond vectors. The BFM has been widely applied to simulate lipid bilayers interacting with homo-polymers [46,47], amphiphilic polymers [48–50] and NPs of various degrees of hydrophobicity [51].

1.5 The Lipid Bilayer Interacting with NPs

NPs or small molecules (cholesterol, alcohols) influence the structural and dynamic properties of the bilayer. Since the membrane is flexible and elastic, it can change its formation to accomodate NPs [52,53]. Identifying the mechanisms of interactions of synthetic NPs with cell membranes is the key for understanding potential NP cytotoxicity [54–56] and for developing efficient applications such as nanocarriers for targeted drug delivery [57,58]. Particularly, it is of great interest to design NPs to breach the free energy barrier imposed by the membrane and to control the translocation of NPs through lipid bilayers.

Experimental and simulation approaches have been implemented to study the interaction of NPs with bio-systems on various timescales, focusing on the effects of NPs' properties, i.e. size, shape, as well as surface chemistry. Recent studies show that charged NPs can alter the local phase state of lipids in the regime in which NPs are binding [59], and also induce membrane disruption [60]. According to molecular dynamics (MD) simulations, membrane pores induced by NPs can change the surface texture of the lipid bilayer [61]. Additionally, the size of the NP is crucial for cell uptake [62–64] and translocation [65]. MD simulation studies of NPs interacting with DPPC [66] and human skin [67] demonstrate that the free energy barrier of translocation through membranes increases with the size of the NP. Apart from the size of the NP, shape and initial orientation can play a role for translocation and cellular uptake [68,69].

As it is difficult to obtain microscopic information about NPs interacting with lipid membranes in experiments, simulations provide valuable physical insight into the interaction of NPs with lipid membranes. However, there still exists a lack of knowledge about the mechanisms behind the translocation process. This concerns in particular the passive transport which does not involve consumption of energy such as ATP-hydrolysis.

1.6 Thesis Overview

In this thesis, MD simulations are implemented to study the lipid membrane interacting with NPs of various hydrophobicity. The main part of this thesis consists of four Chapters. The background and motivation that lead to this work are introduced in this Chapter. The second Chapter starts with a brief introduction of the principle of MD simulations, including the force fields, equations of motion and the related integrations, followed by the description of the barostats and the thermostats that are implemented in this work to keep constant pressure and temperature, and finally the descriptions of umbrella sampling simulation and weighted histogram analysis method are given.

The third and fourth Chapters represent the most important outcomes of the present work. In Chapter3, we implement a simplified MARTINI coarse-grained model to study the interaction between the lipid bilayer and NPs of various hydrophobicity. The scope of this work is to gain insight and understanding of the free energy for NPs' translocation and the influence of NPs on the membrane. Chapter4can be summarized in terms of three aspects: the first concerns the oxidation effects on the lipid membrane. The second is related to

the understanding of the translocation process of NPs through the oxidized lipid bilayer. The third is to determine the oxidized membrane perturbation induced by NPs of various degrees of hydrophobicity. In Chapter5, we summarize the work and give an outlook.

2 State of the art

2.1 Molecular Dynamics Simulations of Lipid Bilayers

Experiments have been conducted for a long time and delivered important findings on biophysics. Despite the fact that different types of lipid membranes and their properties have been extensively studied by experimental methods in last decades [30,70], detailed information is not always accessible. Computer simulations involve the implementation of virtual and numerical experiments, which provide an alternative paradigm to comprehend the observations in experiments and are sometimes able to predict future experimental results. In the scheme of simulations, a variety of simulation methods has been developed, such as molecular dynamics (MD) simulation, Monte Carlo (MC) method and density-functional theory. MD approach, as an important tool, is commonly used to study subjects in chemical physics and biology [71]. In many cases, MD simulations can complement experiments, such as NMR. In addition, different properties can be efficiently evaluated by MD simulations, especially dynamic quantities that can not be generated by other computer simulation techniques, such as MC simulations [72]. In this thesis, MD simulations are conducted to investigate various properties of the lipid bilayers and their interactions with spherical NPs, using the MARTINI model. The MARTINI model, as introduced in Chapter1, can reproduce more realistic membranes which can be mapped to real time and length scales, contrary to the BFM [46,47] by MC simulations. In the BFM, as mentioned in Chapter1, being a lattice model, the NP is considered as a small tetrahedron that is composed by four monomers (cubes)[51]. And in this work, the NP is a CG sphere, as common in continuum space models as well as in nature. Though differences exist between the MARTINI model (MD simulations) implemented in this thesis and BFM [46, 47] (MC simulations), both of them can be used to study and improve the understanding of biological systems.

Initially, simulations of bilayers were only available on time scales of the order of 10

picoseconds [73,74]. With the development of the computational performance and simulation methodologies, to date MD simulations can access in the order of a few hundreds of nanoseconds and nanometers in length. MD simulations reproduce the dynamics of the system and measurements of several properties of the single system. In this thesis, statistical properties are mainly calculated from time-average of a single trajectory during a long time simulation, rather than from many trajectories of various independent systems. These structural quantities computed in our studies, such as the area per lipid and thickness of the bilayer, are averaged from the positions of particles at certain time steps. According to the ergodic hypothesis, it is assumed that the time-average of the quantities of the system is identical to the average over the statistical ensemble, which is stated as follows:

$$< A >= \lim_{\tau \to \infty} \frac{1}{\tau} \int_0^\tau A dt, \tag{2.1}$$

where <> denotes the average over the ensemble, and τ is the simulation time. In this way, configurations of all possible energies will be sampled when the simulation time is sufficient to capture the typical behavior of the system under investigation.

2.1.1 Equations of Motion and the Integrations of Equations of Motion

The basic idea behind MD simulations is integrating the classical Newton equation, which provides the trajectories of particles under a specific force field along the simulation time. In principle, this approach relies on integrating the Newtonian equations of motion for all the particles in the investigated system [75]:

$$m_i \frac{d^2 \mathbf{r}_i}{dt^2} = \mathbf{F}_i, \tag{2.2}$$

where m_i and $\mathbf{r}_i$ denote the mass and position of the i_{th} particle, respectively, and $\mathbf{F}_i$ is the total force acting on it. Generally, the force is derived from the potential energy with respect to the position of the particle:

$$\mathbf{F}_i = -\frac{\partial U(\mathbf{r}_i)}{\partial \mathbf{r}}. \tag{2.3}$$

Knowing the potential energy $U(\mathbf{r})$, the force can be calculated and the new positions are generated further. Due to the fact that Newton equation can only be solved numerically and integrated over discrete times, the performance of MD simulations for a many-particle system heavily relies on the integration algorithm and the time step. To address these issues, several integrators have been developed to numerically integrate Newton equation and maintain energy conservation even on large time scales. With the development of algorithms and computational power, to date simulations of large systems on large time scales can be reached.

In MD simulations, the energy over long simulation time is desired to be conserved, which is ensured by proper integration algorithms. The simplest one, the Euler algorithm [76], yields the velocity and position of particle in the next step, as

$$\begin{aligned} \mathbf{v}(t+\Delta t) &= \mathbf{v}(t) + \mathbf{a}(t)\Delta t \\ \mathbf{r}(t+\Delta t) &= \mathbf{r}(t) + \mathbf{v}(t)\Delta t, \end{aligned} \tag{2.4}$$

where $\mathbf{v}(t)$ denotes the velocity of particle at time t, and $\mathbf{a}(t)$ is the corresponding acceleration. For the Euler algorithm, the truncated Taylor expansion of the particle coordinates contains the first linear component.

A more accurate but also simple algorithm, Verlet integrator [77] is implemented to integrate the equations of motion:

$$\begin{aligned} \mathbf{v}(t+\Delta t) &= \mathbf{v}(t) + \frac{1}{2}\Delta t[\mathbf{a}(t) + \mathbf{a}(t+\Delta t)] \\ \mathbf{r}(t+\Delta t) &= \mathbf{r}(t) + \mathbf{v}(t)\Delta t + \frac{1}{2}\mathbf{a}(t)\Delta t^2. \end{aligned} \tag{2.5}$$

Based on Verlet algorithm, another popular algorithm, known as leapfrog integrator [78], is developed as follows:

$$\begin{aligned} \mathbf{v}(t+\Delta t/2) &= \mathbf{v}(t-\Delta t/2) + \mathbf{a}(t)\Delta t \\ \mathbf{r}(t+\Delta t) &= \mathbf{r}(t) + \mathbf{v}(t+\Delta t/2)\Delta t, \end{aligned} \tag{2.6}$$

The value of time step is one of the most important parameters in MD simulations, which determines the accuracy of the approximated ensemble average. The time step Δt should be small enough that the energy of the systems is conserved within the accuracy needed for the particular study. The proper time steps for the integrations regarding atomistic

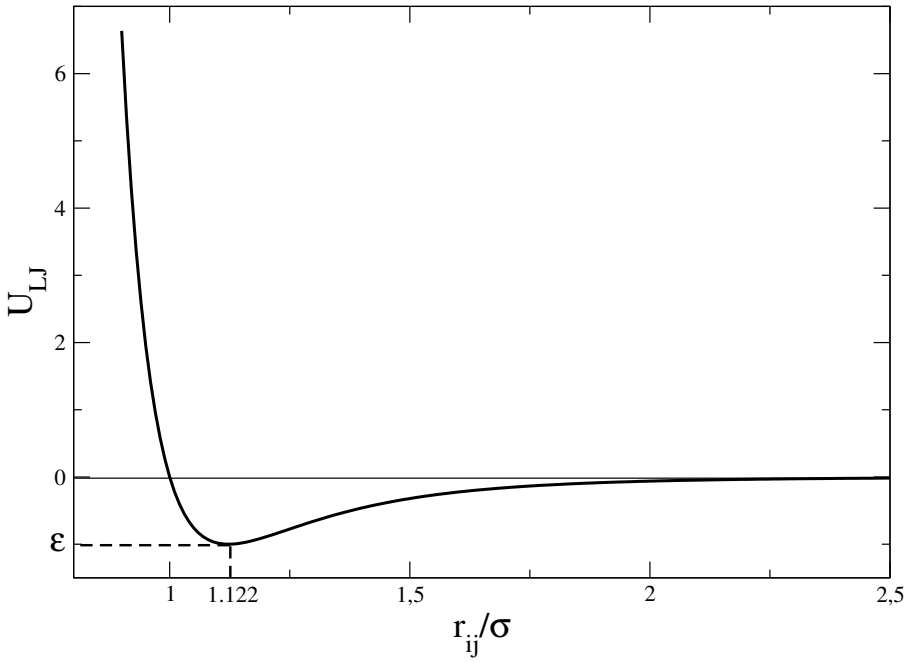

Figure 2.1: Lennard-Jones potential.

and CG MD simulations are often chosen between $2 - 50$ fs to ensure accurate ensemble average. Note that the Verlet algorithm can be implemented to generate not only energetic conservation ensembles, but also constant temperature or constant pressure ensembles.

2.1.2 Interaction Potentials

The interaction potentials determine the forces acting on each particle and characteristics of the system, which is fundamental for models that reproduce real substances. The parametrization of the interactions between particles in MD simulations is called force field. The total potential energy, U, in Eq.2.3, is generally made up of three components, resulting from non-bonded interactions, $U_{\text{non-bonded}}$, bonded interactions, U_{bonded} and external potentials, U_{ext}, under certain constraints (fixed bonds or angles), as:

$$U = U_{\text{non-bonded}} + U_{\text{bonded}} + U_{\text{ext}}. \tag{2.7}$$

A commonly used short-range non-bonded potential, $U_{\text{non-bonded}}$, is the Lennard-Jones (LJ) potential, which is sketched in Figure2.1. It describes the van der Waals interaction in the short range, as:

$$U_{\text{LJ}} = 4\epsilon \left[\left(\frac{\sigma}{r_{ij}} \right)^{12} - \left(\frac{\sigma}{r_{ij}} \right)^{6} \right], \tag{2.8}$$

where the parameters ϵ governs the strength of interaction and σ stands for the effective minimum distance between two particles. The first term $\left(\frac{\sigma}{r_{ij}}\right)^{12}$ is modelling the short range repulsion between two particles. To save computational effort, it is set to be quadratic to the second term $\left(\frac{\sigma}{r_{ij}}\right)^{6}$. The second term dominates the attractive interaction and stands for the induced dipole interaction. It is easy to verify that this potential has a minimum at $r_{min} = 2^{1/6}\sigma$ with a depth $U_{LJ}(r_{min}) = -\epsilon$. Usually, a cutoff is implemented to the non-bonded potential $U_{\text{non-bonded}}$ to reduce the number of pair-pair interaction calculated in MD simulations. LJ interactions are typically truncated at a distance of $r_c = 2.5\sigma$.

The long-range non-bonded interaction is described by the Coulomb interaction for the electric potential of charged particles, given by

$$U_{\text{Coulomb}} = \frac{q_i q_j}{4\pi\epsilon_0\epsilon_1 r_{ij}}, \tag{2.9}$$

where q_i, q_j, ϵ_0, ϵ_i and r_{ij} describe the charge of i and j particles, dielectric constant in vacuum and relative dielectric constant, the relative distance between particles i and j. In addition, particle Ewald summation is introduced to accurately calculate the Coulomb interaction in periodic boundary conditions [79].

The bonded potential, U_{bonded}, has general components of bond potential, U_{bond}, and angle potential, U_{angle}, which is often expressed by a harmonic potential to mimic the spring-like nature, given as follows:

$$\begin{aligned} U_{\text{bond}} &= \frac{1}{2} k_{bond}(b - b_0)^2 \\ U_{\text{angle}} &= \frac{1}{2} k_{angle}(\theta - \theta_0)^2. \end{aligned} \tag{2.10}$$

The external potential U_{ext} accounts for the forces which do not depend on the particle coordinates.

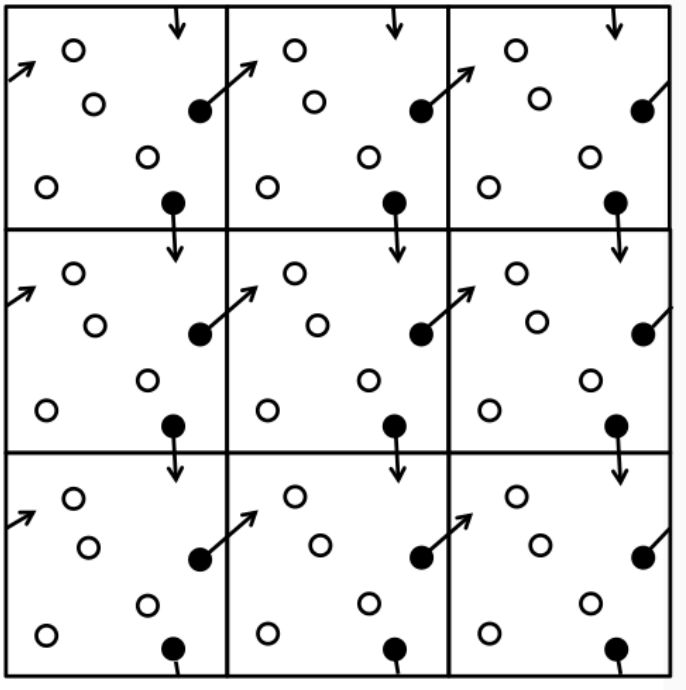

Figure 2.2: Periodic boundary conditions in two-dimensions.

2.1.3 Periodic Boundary Conditions

In realistic systems, often only a small fraction of particles is located at the boundaries, so that the effect of boundary almost plays an insignificant role. However, in MD simulations, generally only a small patch of the sample is accessible, indicating a larger fraction of particles located at the boundaries. Finite systems behave differently from the infinite systems. To overcome this problem, it is possible to apply periodic boundary conditions to a small sample which contains thousands of particles, in order to simulate the bulk system and eliminate surface effects when those are of little interest.

The basic idea behind periodic boundary conditions is that particles are enclosed in a unit box (cell), which is surrounded by several duplications of itself (so called image boxes). Particles in the image box behave identically as those in the original box. When a particle moves out of the unit box from the right, and at the same time the image of the particle enters into the unit box from the left image box, as shown schematically in Figure2.2, such that the number of particles in the unit box is always conserved. Thus, the effect of

boundary is eliminated.

Using periodic boundary conditions implies that particles in the simulation box not only interact with other particles in the unit box, but also with the images of themselves. As a consequence, the effect of periodic boundary conditions should be taken into account in the calculation of the pair-pair interaction and the integration of Newton's equation. This leads to the fact that the pairs of interactions increase significantly when considering the particles both in the unit and image boxes. To address this problem, a potential with a finite range (cutoff) is typically used in the simulations, i.e. ignoring the interactions between two particles that are far away from each other. Another concern is that at each time step, the positions of the particles should be adjusted for the integration of Newton's equation. If the particle is located at the left/right side of the unit box, the position is readjusted as follows to bring the particle back to the unit box:

$$\begin{aligned} x &= x + L_x, when\ x < 0; \\ x &= x - L_x, when\ x > L_x. \end{aligned} \tag{2.11}$$

where x and L_x are the position of particle in x direction and the length of box in x-coordinate, respectively. Note that the size of the simulation box should be sufficient large to avoid the finite size effects of the boundary. Typically, the box should be at least larger than twice of the cutoff length for the pair interaction, otherwise a particle can interact with its image in the neighboring box. This can induce significant unphysical dynamics.

2.1.4 Barostats and Thermostats

In MD simulations, a variety of different methodologies has been introduced to generate not only NVE ensembles (i.e. microcanonical ensembles, fixed number of particles N, volume V and energy of the system E), but also NVT ensembles regarding fixed number of particles N, volume V and temperature T, and NPT ensembles associated with a constant number of particles N, pressure P and temperature T in the system. It is common to implement the isothermal-isobaric ensembles (NPT) to mimic realistic lipid membranes (condensed phase system) in experiments. Early pioneering work was introduced by Berendsen, who proposed a method to maintain constant pressure by scaling the coordinates and the volumes of the system [80]. Being inspired by Andersen's work [81], a more sophisticated methodology to generate desired constant pressure ensembles was developed by Nóse and later reformulated

by Hoover [82], in which an additional degree of freedom was introduced. The Nóse-Hoover barostat was further refined by Martyna et al [83]. We note that for the study in Chapter3, the simulations were conducted with a Langevin thermostat as described in Ref. [84] and a Berendsen barostat [80] to control the temperature and pressure. Simulations in Chapter4 are conducted with a Martyna-Tuckerman-Tobias-Klein barostat.

Langevin Thermostat

In the Langevin thermostat, the movement of particles is driven by the stochastic noise term $\xi(t)$ in the force as follows:

$$m\frac{d^2\mathbf{r}}{dt^2} = -\frac{\partial U(\mathbf{r})}{\partial \mathbf{r}} - m\gamma\frac{d\mathbf{r}}{dt} + \xi(t), \tag{2.12}$$

where m, $\mathbf{r}$, t, γ and $\xi(t)$ are the mass, the position of particle, the simulation time, the friction coefficient and the random force that gives random kicks to the particles. The average magnitude of the random force and the friction are connected according to the “fluctuation-dissipation" theorem. Note that the random force is time and position uncorrelated:

$$< \xi_i(t)\xi_j(t') >= 2\gamma m k_B T \delta_{ij}\delta_{t,t'}, \tag{2.13}$$

In this way, each particle is coupled to a heat bath. This allows to use a larger time step compared to a non-stochastic thermostat, and the Langevin thermostat is frequently used in implicit solvent models. However, the momentum in the Langevin thermostat is not conserved, which implies that it does not reproduce all dynamic properties, such as hydrodynamic interactions.

Berendsen Barostat

A microscopic expression for the pressure of a mechanical system can be denoted by [80]:

$$\begin{aligned} P &= \frac{Nk_BT}{V} - \left(-\frac{1}{3V}\sum_i \mathbf{r}_i \cdot \mathbf{F}_i\right) \\ &= \frac{1}{3V}\sum_i \left[\frac{{\mathbf{p}_i}^2}{m_i} - (-\mathbf{r}_i \cdot \mathbf{F}_i)\right], \end{aligned} \tag{2.14}$$

where N, V, $\mathbf{r}_i$, $\mathbf{F}_i$, $\mathbf{p}_i$ and m_i are the number of particles, the volume of the system, the position, force acting on the particle, the momentum and the mass of i_{th} particle, respectively.

The basic idea of Berendsen barostat is to obtain the desired pressure by scaling the volume of the system and the positions of particles. The Berendsen barostat is a weak coupling method, which resets the pressure of the system by rescaling the volume of the system and the atom coordinates with a factor of $\eta^{1/3}$ for every time step [80]:

$$\mathbf{r}' = \eta(t)^{1/3}\mathbf{r},\ with\ \eta(t) = 1 - \frac{\delta t}{\tau_P}\kappa(P_0 - P(t)), \tag{2.15}$$

where $\mathbf{r}$, η, and $\kappa = -\frac{1}{V}(\frac{\partial V}{\partial P})_T$ are the coordinates, the relative scaling parameter and the isothermal compressibility of the system. The parameters $P(t)$ and P_0 are the instantaneous pressure and target pressure, respectively. Typically, a value of κ in the order of $10^{-4} \sim 10^{-3}$ bar^{-1} is set for the MARTINI model.

In isotropic systems, the scaling factors in x, y and z directions are identical. Vice versa, in anisotropic systems, different scaling factors η are used for x, y and z directions. In our studies, the pressure is coupled in x and y directions to minimize the stress of the membrane, i.e. the scaling factor in x and y directions are identical.

The equation of motion for constant pressure ensemble generated by the Berendsen barostat [80] is given by

$$\frac{dP(t)}{dt} = \frac{P_0 - P(t)}{\tau_P}, \tag{2.16}$$

where τ_P is the relaxation time coupled with the external bath. The parameter τ_P is specified in the simulation and denotes the strength of the coupling between the system and the pressure bath. In simulations, a proper relaxation time τ_P is important. Large τ_P indicates a weak coupling, which leads to a long simulation time for the system to reach equilibrium. On the other hand, small τ_P could induce a strong influence on the dynamics of the system.

Using a Berendsen barostat, the system reaches a desired pressure rather quickly. It yields correct average quantities. However, the fluctuations of the quantities are suppressed. When using a Berendsen barostat in LAMMPS, the time integration and the processes of rescaling the box size and atom coordinates according to the barostat are separated. Therefore, in the simulations conducted in Chapter3, a Langevin thermostat is required

to control the temperature and update the positions and velocities of atoms.

Martyna-Tuckerman-Tobias-Klein (MTTK) Barostat

In the implementation of a Berendsen barostat, a proper average pressure P is generated, but the fluctuation of the pressure is suppressed [85]. Another methodology to keep pressures constant was proposed by Anderson [81]. The idea of the Anderson scheme is to reformulate the Lagrangian equations of motion by introducing an additional variable V, the volume of the simulation box, which acts as the coordinate of a “piston" connected to the external desired pressure. The “piston" has a “mass", Q, which is critical and adjustable. Too small values of Q can induce rapid oscillations of the simulation box size, while a large Q may lead to no change of the volume. In this implementation, the method can generate a isobaric-isothermal distribution in the phase space.

Based on the Anderson scheme, Nóse and Hoover extended the Lagrangian and added new degrees of freedom, i.e. introducing dynamic variables that are coupled to the velocities of particles. The Nóse-Hoover implementation leads to strong oscillations when the starting point of pressure is far from the desired value. Compared with Nóse-Hoover barostat, MTTK implementation improves the ergodicity of the systems by thermostatting the thermostat variable [86], i.e. implementing a chain of Nóse-Hoover thermostats. Additionally, it is time-reversible and allows backwards-propagation of the system.

For the MTTK barostat, the equations of motion in d dimensions are defined as follows [83, 86]:

$$
\begin{aligned}
\dot{\mathbf{r}}_i &= \frac{\mathbf{p}_i}{m_i} + \frac{p_\epsilon}{W}\mathbf{r}_i, \\
\dot{\mathbf{p}}_i &= \mathbf{F}_i - (1 + \frac{d}{dN})\frac{p_\epsilon}{W}\mathbf{p}_i - \frac{p_\xi}{Q}\mathbf{p}_i, \\
\epsilon &= \ln(V/V_0), \\
\dot{V} &= \frac{dVp_\epsilon}{W}, \\
\dot{p}_\epsilon &= dV(P_{int} - P_{ext}) + \frac{1}{N}\sum_{i=1}^{N}\frac{\mathbf{p}_i^2}{m_i} - \frac{p_\xi}{Q}p_\epsilon, \\
P_{int} &= \frac{1}{dV}[\sum_{i=1}^{N}(\frac{\mathbf{p}_i^2}{m_i} + \mathbf{r}_i \cdot \mathbf{F}_i) - dV\frac{\partial U(\mathbf{r}, V)}{\partial V}].
\end{aligned}
\tag{2.17}
$$

where N, $\mathbf{r}_i$, $\mathbf{p}_i$, V, V_0 and $U(r, V)$ are the number of particles, position and momentum of

the i_{th} particle, the volume, the initial box size and the potential. $\mathbf{F}_i$ is the force derived from the potential $U(\mathbf{r}, V)$. The parameters P_{int} and P_{ext} denote the internal pressure that is calculated during the simulation and the external/desired pressure. The variables ξ, p_ξ and Q are conjugated to the thermostat. Whereas, ϵ, p_ϵ and W are associated with the barostat. Here, Q and W are the mass of thermostat and barostat, respectively.

2.2 Umbrella Sampling Simulation

The free energy is one of the most important quantities in thermodynamics. Many biological/chemical processes and physical phenomena are related with the free energy difference. The sign of the free energy difference determines whether a reaction is spontaneous or not. In the study of this thesis, free energy barriers determine the frequency of NPs translocation through the bilayers. Usually, for NVT ensemble, the free energy is expressed in terms of the so-called Helmholtz free energy, vice versa, for NPT ensemble, the Gibbs free energy is used. Since most experiments are usually conducted under the conditions of constant temperature and pressure, the study of Gibbs free energy is of great interest.

In principle, the free energy profile along the reaction coordinate, known as the potential of mean force, can be directly calculated from simulations. Here, the reaction coordinate (ξ), is a continuous parameter which provides a distinction between two thermodynamic states. However, in many cases simulations do not provide enough samples in the high-energy region of phase space within the finite simulation time. Obtaining the free energy can be a difficult task in computational biology and physics. Different sophisticated techniques are developed for this purpose, *e.g.* thermodynamic integration and free energy perturbation for calculating the free energy difference between two states [86,87] and umbrella sampling [88, 89].

The umbrella sampling technique was developed by Torrie and Valleau in 1977 [88,89], who were inspired by the work of McDonald [90,91]. To date, the applications of umbrella sampling simulations range from providing understanding of chemical reactions, calculating conformational free energies of peptides/biomolecules and exploring opportunity of drug delivery, to name a few of them. In this work, we implemented umbrella sampling simulations to study the free energy landscapes along the membrane regarding the NPs' translocation. Therefore, in this section, we briefly describe the basics of umbrella sampling technique, further demonstrate how to analyze umbrella sampling simulation results,

and finally clarify the principle of the bias potential applied in the umbrella sampling simulations.

2.2.1 The Basics of Umbrella Sampling Method

In principle, the free energy profile can be directly obtained from the simulation when the simulation time is sufficiently long to sample the whole phase space. With the reaction coordinate ξ defined, the partition function of the system $Q(\xi)$ can be calculated by integrating out all degrees of freedom but ξ:

$$Q(\xi) = \frac{\int exp[-\beta E(r)]\delta[\xi^{'}(r) - \xi]d^N(r)}{\int exp[-\beta E(r)]d^N r}, \tag{2.18}$$

where $\beta = 1/(k_B T)$, r and $E(r)$ are the coordinate and the potential energy, respectively. The reaction coordinate ξ can be expressed as a function of a distance, an angle or other variables related to the system. In our study, ξ refers to the distance between the center of the membrane and the NP. The free energy along the reaction coordinate, so-called the potential of mean force (PMF), is given by

$$A(\xi) = -1/\beta \ln Q(\xi). \tag{2.19}$$

In principle, $A(\xi)$ can be directly obtained from MD simulations by monitoring $Q(\xi)$, the probability distribution of the system along the reaction coordinate. Typically, for a coarse-grained MD simulation, a length scale of hundreds of nanometers and a time scale of hundreds of nanoseconds can be reached. However, interesting phenomena in biology (NP translocation event) require longer time and occur at low probability, which indicates that it may be impossible to observe such phenomena in the direct simulation. The low probability of overcoming the potential barrier can leave configurations in high energy-region poorly sampled or even entirely non-sampled by the simulation. It is infeasible to directly sample states with an energy barrier significantly larger than $k_B T$.

The basic idea of umbrella sampling is applying a bias potential to the system in order to ensure efficient sampling along the whole reaction coordinate. This additional bias potential can be applied in one simulation (window) or in various separated simulations along the reaction coordinate which have sufficient overlap between neighbor windows and can subsequently be assembled by different methods. In this work, umbrella sampling

simulations are performed in many windows along the reaction coordinate ξ, which can be formalized as follows [92]:

$$E^{biased}(r) = E^{unbiased}(r) + w_i(\xi), \tag{2.20}$$

where $E^{biased}(r)$ and $E^{unbiased}(r)$ denote the biased free energy and unbiased free energy at the position (or state) r, and $w_i(\xi)$ being the bias (additional) potential.

The aim is to obtain the unbiased free energy, which is related to the unbiased distribution by the equation:

$$P_i^{unbiased}(\xi) = \frac{\int \exp\{-\beta[E(r)]\}\delta[\xi^{'}(r) - \xi]d^N r}{\int \exp\{-\beta[E(r)]\}d^N r}. \tag{2.21}$$

However, only the biased distribution can be directly extracted from the biased MD simulations as follows:

$$P_i^{biased}(\xi) = \frac{\int \exp\{-\beta[E(r) + w_i(\xi^{'}(r))]\}\delta[\xi^{'}(r) - \xi]d^N r}{\int \exp\{-\beta[E(r) + w_i(\xi^{'}(r))]\}d^N r}. \tag{2.22}$$

As seen in Eq.2.22, the biased distribution is also a function of the reaction coordinate ξ. This equation can be further modified as

$$P_i^{biased}(\xi) = \exp[-\beta w_i(\xi)]\frac{\int \exp\{-\beta[E(r)]\}\delta[\xi^{'}(r) - \xi]d^N r}{\int \exp\{-\beta[E(r) + w_i(\xi^{'}(r))]\}d^N r}. \tag{2.23}$$

By inserting in Eq.2.21, we can obtain the relation between the unbiased distribution $P_i^{unbiased}(\xi)$ and biased distribution $P_i^{biased}(\xi)$:

$$\begin{aligned} P_i^{unbiased}(\xi) &= P_i^{biased}(\xi)\ \exp[\beta w_i(\xi)]\frac{\int \exp\{-\beta[E(r) + w_i(\xi^{'}(r))]\}d^N r}{\int \exp\{-\beta[E(r)]\}d^N r} \\ &= P_i^{biased}(\xi)\ \exp[\beta w_i(\xi)] < \exp[-\beta w_i(\xi)] > \\ &= P_i^{biased}(\xi)\ \exp[\beta(w_i(\xi) - F_i)], \end{aligned} \tag{2.24}$$

In our study, the path along the reaction coordinate is discretized into a number of windows (for instance, $\xi = 26, 31, 38$), as shown in the upper panel of Figure2.3(red lines). The computed biased free energy, unbiased free energy and bias potential are denoted as blue, green and red lines in the middle panel of Figure2.3, respectively.

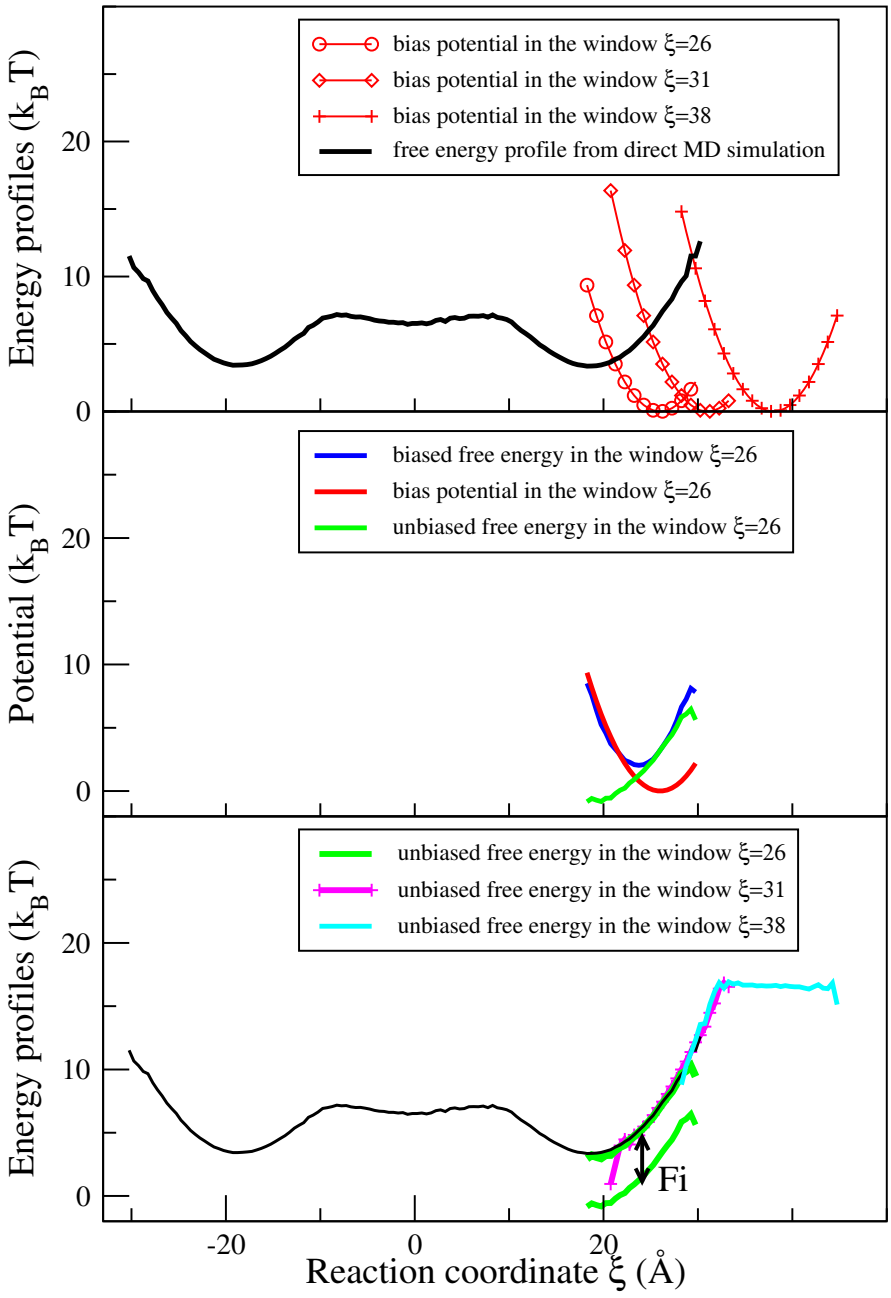

Figure 2.3: Bias potential applied in windows along the reaction coordinate (upper panel). Biased free energy, bias potential and unbiased free energy in the window $\xi = 26$ (middle panel). Global free energy composed of direct MD simulation result and unbiased free energy in each window (lower panel).

2.2.2 Analyzing Umbrella Sampling Results by WHAM

To analyze the umbrella sampling simulation results, the Weighted Histogram Analysis Method (WHAM) was applied to obtain the global distribution of the free energy. The WHAM is the extension of the histogram technique developed by Ferrenberg and Swendsen [93]. It was first applied in the free energy calculation in Ref. [94]. The goal of WHAM is to minimize the statistical errors when generating the optimal global distribution, in which sufficient overlap between neighboring windows is required. In other words, to choose appropriate parameter values of F_i in Eq.2.24for each window, as sketched in the down panel of Figure2.3.

The global distribution can be constructed by the unbiased free energy from each window according to different weights $p_i(\xi)$ [92,94,95]:

$$P^{unbiased}(\xi) = \sum_{i}^{N_{windows}} p_i(\xi) P_i^{unbiased}(\xi). \tag{2.25}$$

The basic idea behind WHAM is to choose the optimum probability density from i_{th} window when it has overlap with neighboring windows. The statistical error of $P^{unbiased}$ in the histograms is then summarized from each window as follows:

$$\sigma^2(P^{unbiased}) = \sum p_i^2(\xi)\sigma^2(P_i^{unbiased}(\xi)) \tag{2.26}$$

When minimizing the statistical error of $P^{unbiased}$, the weights $p_i(\xi)$ of each window are required for the normalization:

$$\frac{\partial \sigma^2(P^{unbiased})}{\partial p_i} = 0, \ with \ \sum p_i(\xi) = 1. \tag{2.27}$$

This leads to $P^{unbiased}(\xi)$ as follows:

$$\begin{aligned} P^{unbiased} &= \sum_{i=1}^{N} \frac{n_i \exp\{-\beta[w_i(\xi) - F_i]\}}{\sum_{j=1}^{N} n_j \exp\{-\beta[w_j(\xi) - F_j]\}} P_i^{unbiased}(\xi) \\ &= \sum_{i=1}^{N} \frac{n_i}{\sum_{j=1}^{N} n_j \exp\{-\beta[w_j(\xi) - F_j]\}} P_i^{biased}(\xi), \end{aligned} \tag{2.28}$$

with n_i the length of the i_{th} window. The free energy parameter F_i is given as follows:

$$\exp(-\beta F_i) = \int d\xi P^{unbiased}(\xi) \exp[-\beta w_i(\xi)]. \tag{2.29}$$

The parameter F_i in Eq.2.29is calculated from the global unbiased distribution $P^{unbiased}(\xi)$, while $P^{unbiased}(\xi)$ is obtained from Eq.2.28using the biased distribution $P^{biased}(\xi)$ and F_i. It should be noted that this process has to form a self-consistent loop, in which the parameters are iterated until convergence.

2.2.3 The Principle of Choosing Bias Potential

To obtain sufficient sampling in the poor-sample region, the choice of the bias/forcing potential introduced in the potential function, is critical in the umbrella sampling simulations. The bias potential has to ensure an appropriate number and position of windows to get sufficient overlap, while not disturbing the system too much.

In many cases and throughout this work, a bias potential in a harmonic format is applied to the system in several windows distributed along the reaction coordinate:

$$w_i(\xi) = \frac{1}{2} K(\xi - \xi_i)^2. \tag{2.30}$$

where K is the spring constant, and ξ_i is the reference point. The choice of the spring constant K is essential. Too large K leads to narrow distributions with no sufficient overlap between two neighboring windows, while small time steps are required in simulations. Another pitfall of large K is that it might lead to the over-representation of configurations in high-energy region. In the other limit, a low value of K may not be enough to overcome the energy barrier, leading to insufficient sampling in the desired region.

3 Lipid Membranes interacting with Nanoparticles of Various Degrees of Hydrophobicity

3.1 Introduction

Nanoparticles (NPs) have various applications in drug delivery, therapeutic and diagnostic applications [96–98]. Specially, gold-coated NPs are good candidates in various biomedical applications due to their resistance against oxidation and corrosion [99]. Diverse properties of NPs, such as the hydrophobicity of NPs, size, shape and surface charge, affect the biological response. The hydrophobicity of NP is an essential parameter controlling the interaction with the membrane. It was reported that NPs with different degrees of hydrophobicity lead to different immune responses [100]. NPs' surface binding with human serum albumin can be tuned by NPs' hydrophobicity [101]. Recent studies show that hydrophobic NPs with diameters comparable to the thickness of a lipid bilayer can affect the phase transition temperature and membrane fluidity [102]. In addition, the bilayer can adjust its assembly to accommodate large hydrophobic NPs [52,53]. Such distortion of the bilayer can, however, reduce the order of the lipid. Similar phenomena are also observed for proteins with large sizes [103].

The self-assembly of lipids into bilayers is driven by the hydrophobic interaction, i.e. the demixing of the hydrophobic tails of the lipids from the aqueous solution. Due to the hydrophobic effect, hydrophobic NPs are easily absorbed in the core of the lipid bilayer. To improve the translocation of NPs, strategies have been applied to modify NPs' surface chemistry, e.g. through the implementation of hydrophobic/hydrophilic patterns on the surface of the NP. Stellacci *et al.* designed NPs coated with alternating hydrophobic and hydrophilic ligands that could penetrate the membrane without inducing membrane

disruption, while NPs randomly decorated with hydrophilic and hydrophobic components got trapped in endosomes [104]. In turn, Gkeka *et al.* performed CG molecular simulations to study the effect of various hydrophobic-hydrophilic surface patterns on the permeation of NPs through lipid membranes [105]. In particular, homogeneously distributed hydrophobic-hydrophilic surface patterns have been demonstrated to flatten the translocation free-energy profiles.

The hydrophobicity of NPs also influences the selectivity of the bilayer. Monte Carlo (MC) simulations of homogeneous/amphiphilic NPs interacting with lipid bilayers show that NPs having a certain degree of hydrophobicity could induce a dramatic increase of the permeability of lipid bilayers for water [106]. Similar results have been reported in recent studies of homopolymers/copolymers of tunable hydrophobicity [107–109]. The analysis of the disruption of supported membranes, induced by semi-hydrophobic NPs, demonstrates that surface hydrophobicity, concentration and size of the NPs control the formation of pores in the membrane. This offers insight into the design of biofunctional NPs with a reduced potential of cytotoxicity [110]. Neutral or negatively charged, polymer-coated AuNPs exhibit an increased rate of crossing the Caco-2 monolayer (of human colon adenocarcinoma cells). These AuNPs were also capable of inducing an elevated cellular monolayer permeability (up to 4 folds) for small molecules [65].

The objective of this work presented in this chapter is to investigate self-assembled lipid bilayers interacting with spherical NPs under various degrees of hydrophobicity and different concentrations of NPs, using a simplified version of the MARTINI model [37]. Sec.3.3.1 provides information of the distributions of NPs of different degrees of hydrophobicity. The effect of hydrophobicity on translocation rate of NPs is discussed in Sec.3.3.2, followed by the analysis of the concentration effect of NPs on the translocation rate (Sec.3.3.3). Different kinetic pathways for NPs with intermediated hydrophobicity are further discussed in Sec.3.3.4. In Sec.3.3.5, the translocation of NPs through lipid membranes is studied in terms of the potential of mean force and Kramers theory. In Sec.3.3.6, the degree of hydrophobicity of the NP is classified in terms of a hydrophobicity scale, which is accessible experimentally. The effect of hydrophobicity and concentration of NPs on the perturbation of membranes is demonstrated in Sec.3.3.7. Our findings are summarized and discussed in Sec.3.4. Essential results of this work have been published in Ref. [111].

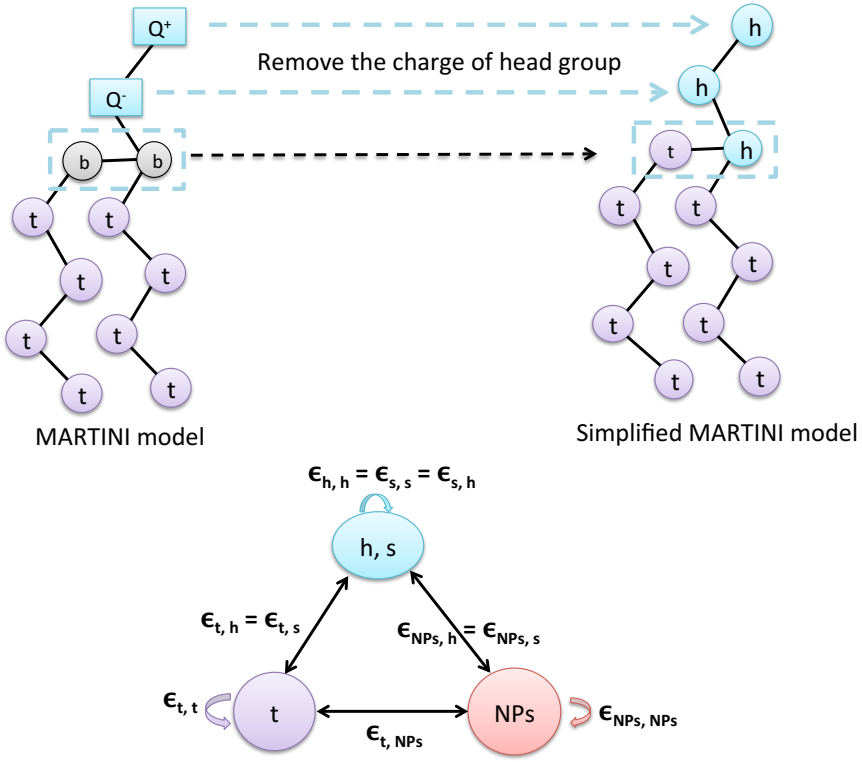

Figure 3.1: Upper panel: Sketch of the MARTINI model and simplified MARTINI model for lipids. Here, Q^+ and Q^- represent the zwitterionic headgroup. And h, t, b, s denote head, tail, bridge monomers of lipids and solvent beads. Lower panel: Sketch of interaction sites.

3.2 Coarse-grained Model and Simulation Setups

In this work, the lipid membrane is constructed using a simplified version of the MARTINI model of DPPC molecules [37]. As mentioned in Chapter1, in the MARTINI model, the lipid molecule consists of 12 CG beads. A CG bead has a mass of 72 amu and is mapped to four heavy atoms. Four types of interactions are considered according to their strengths: polar (solvent), nonpolar (bridge), apolar (tail) and charged (head). The zwitterionic head group is composed of a positively charged bead and a negatively charged bead. The monomers (bridge) placed between zwitterionic head group and tail group are modeled by nonpolar beads.

Figure3.1presents the structure of the lipid molecule, as used in the present work (upper

	Simplified MARTINI model	MARTINI model
Area per lipid	61 $Å^2$	64 $Å^2$
Thickness	44 Å	40 ± 1 Å
Stretching modulus	400 mN/m	400±30 mN/m
Permeation rate of solvent	7.5×10^{-3} cm/s	$(1.5 \pm 0.5) \times 10^{-3}$ cm/s

Table 3.1: Characteristics of lipid bilayers constructed by original MARTINI model and simplified MARTINI model.

panel), as well as the interaction sites for NPs of tunable degrees of hydrophobicity, H (lower panel). The simplified model consists of a reduction in the bead types to only two different neutral bead-species, namely apolar lipid tails and polar lipid heads. The charge of the head group is not included in this study and the bridge beads (nonpolar) are signed to tail and head monomers. Therefore, lipid head monomers and solvent beads are identical in terms of hydrophobic interactions. Minimal models of this type (lipids consist of only two different types of beads) have been successfully applied in recent bond-fluctuation based MC simulations [107–109].

The bond potential for two connected beads is implemented by a harmonic potential:

$$U_{\text{bond}} = \frac{1}{2} k_{bond} (b - b_0)^2, \tag{3.1}$$

where the equilibrium distance b_0 is 4.7 Å and a spring constant of $k_{bond} = 1250$ kJ mol^{-1} nm^{-2} is used. The angle potential with a spring constant of $k_{angle} = 25$ kJ mol^{-1} rad^{-2} is used to model the chain stiffness:

$$U_{\text{angle}} = \frac{1}{2} k_{angle} (\cos(\theta) - \cos(\theta_0))^2 \tag{3.2}$$

Here, the equilibrium angle θ_0 is 180 ° for the lipid tail and head regions. And a smaller equilibrium angle of 120 ° is implemented in the backbone head(Q^+) − bridge − bridge.

A comparison of simplified MARTINI model and original MARTINI model for properties of lipid membranes is shown in Table.3.1. With the simplified MARTINI model, the properties of lipid membranes are in the range of experimental values. Note that the stretching modulus of the membrane was calculated in the presence of 450 lipids with the MTTK barostat as described in Chapter2. The stretching modulus regarding MARTINI model is, instead, obtained from a system consisting of 256 lipids [37]. The permeation rate of water obtained in our model is higher than the result from the MARTINI model, but

agrees with the magnitude of water permeation rate in experimental measurements [112, 113] regarding DPPC vesicles and simulation results of DPPC bilayers [114]. Therefore, the simplified model can reproduce essential properties of real systems. The objective of this work was, however, to study the generic effect of relative hydrophobicity on the interaction of NPs with lipid bilayers. Charge effects of the lipid head group, although substantially screened under physiological conditions, can be investigated as an additional parameter in future studies and can be important for charged particles.

The effective interaction potentials between NPs of various hydrophobicities and components of the system are implemented as follows (as shown in the lower panel of Figure3.1):

$$
\begin{aligned}
U_{LJ}(r) &= 4\epsilon_{ij}\left[\left(\frac{\sigma_{ij}}{r}\right)^{12} - \left(\frac{\sigma_{ij}}{r}\right)^{6}\right], \\
&\sigma_{i,j} = (D_i + D_j)/2, \\
&\epsilon_{h,h} = \epsilon_{s,s} = \epsilon_{h,s} = 5 \text{ kJ/mol}, \\
&\epsilon_{t,t} = 3.4 \text{ kJ/mol}, \\
&\epsilon_{t,h} = \epsilon_{t,s} = 1.8 \text{ kJ/mol}, \\
&\epsilon_{NP,NP} = \epsilon_{s,s} + (\epsilon_{t,t} - \epsilon_{s,s}) \times H, \\
&\epsilon_{NP,h} = \epsilon_{NP,s} = \epsilon_{s,s} + (\epsilon_{t,s} - \epsilon_{s,s}) \times H, \\
&\epsilon_{NP,t} = \epsilon_{s,t} + (\epsilon_{t,t} - \epsilon_{s,t}) \times H.
\end{aligned}
\tag{3.3}
$$

Here, lipid head monomers, tail monomers, and solvent beads are denoted by h, t and s respectively. Note that the diameter of a NP ($D_{NP} = 9.4$ Å) is twice the diameter of a coarse-grained lipid monomer ($D_{s,h,t} = 4.7$ Å) or a coarse-grained water bead. Thus, the effective interaction lengths of the Lennard-Jones potentials of NP-NP and NP-other components are $\sigma_{NP,NP} = 9.4$ Å and $\sigma_{NP,(s,h,t)} = 7.05$ Å, respectively. When the NP is hydrophilic ($H = 0$), its interactions are identical with those of the solvent beads and the lipid head monomers. Vice versa, interactions of hydrophobic NPs ($H = 1$) are indistinguishable from lipid tail monomers. Here, the interaction between NPs also varies when their hydrophilicity is shifted. For hydrophilic NPs with $H = 0$, the NP-NP interaction is equal to the solvent-solvent interaction ($\epsilon_{NP,NP} = \epsilon_{s,s} = 5$ kJ/mol), and $\epsilon_{NP,NP} = \epsilon_{t,t} = 3.4$ kJ/mol for hydrophobic NPs with $H = 1$. Therefore, the hydrophobicity of NPs can be defined as follows:

$$
H = \frac{\epsilon_{NP,NP} - \epsilon_{s,s}}{\epsilon_{t,t} - \epsilon_{s,s}} = \frac{\epsilon_{NP,h} - \epsilon_{s,s}}{\epsilon_{t,s} - \epsilon_{s,s}} = \frac{\epsilon_{NP,t} - \epsilon_{s,t}}{\epsilon_{t,t} - \epsilon_{s,t}}. \tag{3.4}
$$

Note that the effective interaction between NPs is always the result of bare interactions and those between the NPs and the other components. Also realistic particles will differ in this respect. Therefore, it is important to introduce a hydrophobicity scale which can be directly applied to experiments, regardless of the details of the microscopic interactions. This is done in Section3.3.6. The simplified MARTINI model used in this work is able to interpolate between maximum degrees of lipophilicity and hydrophilicity, and thus serves to study these effects using a single parameter, H.

The simulations were conducted with the open source LAMMPS molecular dynamics package [115], using highly parallelized codes. To model the membrane, an initial configuration of 450 lipid molecules was assembled and arranged into a planar lipid bilayer in the $x-y$ plane, while solvent beads and NPs were randomly distributed outside the lipid membrane. An (initially) cubic simulation box of 120 Å and periodic boundary conditions in all directions were implemented. For systems in the presence of 50 and 100 NPs, 8653 and 8253 solvent beads were simulated, respectively. A simulation of 300 ns (10^7 MD steps) was used for the equilibration of a tensionless membrane, with a constant time step of 30 fs. It was followed by a production run of 2700 ns ($9 * 10^7$ MD steps). The temperature of the system was coupled to a Langevin thermostat (temperature 323 K) and the pressure was coupled to a Berendsen barostat [80] (water pressure 1bar, with a bulk modulus of the membrane of 3333.3 bar). The technical details of the thermostat and barostat are described in Chapter2. Note that the barostat was coupled to the $x-y$ plane of the membrane, to respond to its stress, while in the z-direction (normal to the membrane) the barostat secured a constant solvent pressure.

In order to obtain the free energy profile of the NPs as a function of their distances to the membrane's center, a series of umbrella sampling simulations were conducted with the LAMMPS package [115]. For umbrella sampling simulations, the NP is constrained by a bias potential to a target position z_0 using a harmonic potential $w_{bias} = (1/2)K(z-z_0)^2$. The spring constant is set to $K = 0.2$ kcal/(molÅ^2). This set up is similar to a tweezer-type experiment, but instead of measuring the force, the distribution of the particle is recorded, $\rho(z)$, under the harmonic constraint. As the center of mass of the membrane is not fixed in the simulations, the relative distance between the membrane's center and constrained harmonic particle was updated during sampling. Umbrella sampling simulation results for different values of z_0 were combined according to the weighted histogram analysis method (WHAM). For the analysis with WHAM, a bin of 0.5 Å and convergence threshold of 0.1 were implemented. Then, all the potential of mean forces of NPs with different

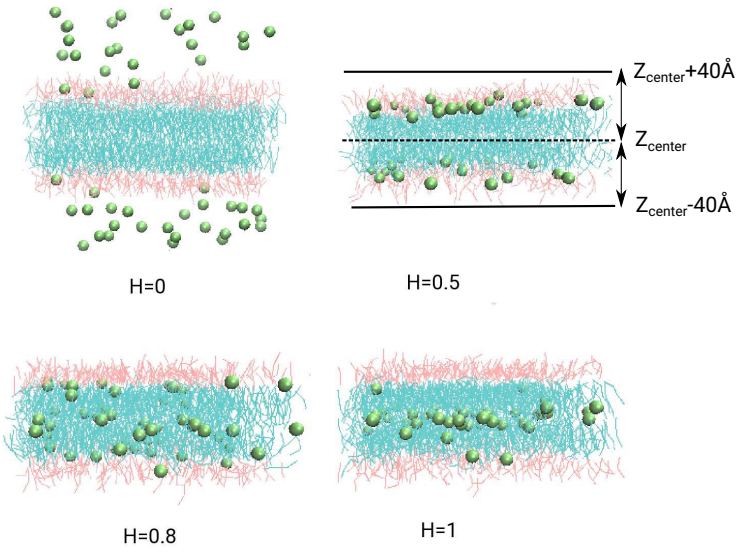

Figure 3.2: Snapshots: Lipid membranes interacting with 50 NPs, at different values of the hydrophobicity ($H = 0, 0.5, 0.8, 1$). Solvent beads are not shown to improve visibility. The solid lines displayed for $H = 0.5$ indicate the thresholds for calculating translocation events. This figure is adopted from Ref. [111]

hydrophobicities were shifted to zero in the region far outside the membrane. Note that in this procedure the bias potential should not perturb the system. As a consequence, the biased samples, after subtracting the harmonic bias potential from the resulting free energy, should lead to the identical result as an unbiased sample, where the histogram of particle positions, $\rho(z)$, has been recorded. This fact can be used when combining biased and unbiased results in overlapping windows of the reaction coordinate, z, whenever this was possible.

3.3 Results and Discussions

3.3.1 NPs-membrane Interactions

NPs of various degrees of hydrophobicity behave quite differently when interacting with the lipid membrane. Multiple systems consisting of lipid membranes interacting with

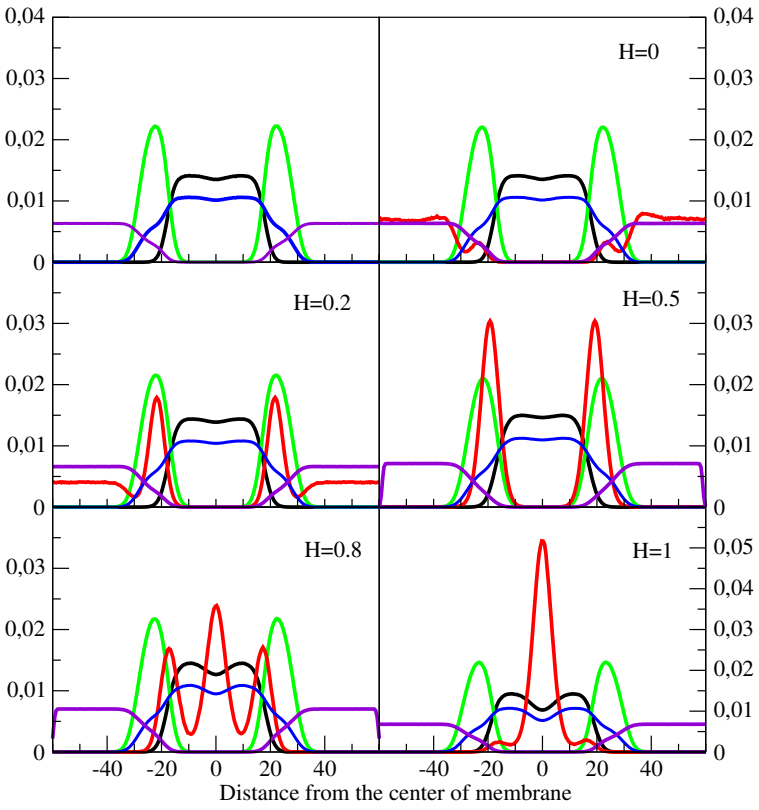

Figure 3.3: Density profiles of the various components of the lipid membrane, as well as the NPs at different degrees of hydrophobicity ($H = 0, 0.2, 0.5, 0.8, 1$). Tail groups (black), head groups (green), lipid molecules (blue), NPs (red) and the solvent beads (purple) are presented as functions of distance from the center plane of the membrane, z. This figure is adopted from Ref. [111]

NPs of hydrophobicity $H = 0, 0.1, 0.2, 0.3, 0.4, 0.5, 0.6, 0.7, 0.8, 0.9$ and 1 are conducted to investigate the effect of hydrophobicity on NPs-membrane interactions. It is well understood that hydrophilic NPs, $H = 0$, are excluded from the lipid bilayer. Upon a further increase of the hydrophobicity to $H = 0.5$, NPs were absorbed on the membrane surface, specifically in the head-tail interface. Hydrophobic NPs ($H = 0.8, 1$) disperse in the core of lipid membrane. Overall, with increasing hydrophobicity from $H = 0$ to $H = 1$, the role of the lipid membrane changes from a potential NP barrier to a potential NP trap. These findings can be clearly observed in the snapshots of lipid bilayers interacting with NPs (see Figure3.2).

To gain more insight into the interactions between lipid membrane and NPs, the corresponding density profiles of all components are analysed and shown in Figure3.3. For

hydrophilic NPs ($H = 0, 0.2$), a depletion zone at the water-membrane interface is observed. This is consistent with previous simulations of membranes and NPs of small diameters, as summarized in a recent review [116]. For NPs with hydrophobicity $H = 0.5$, the distribution shows two distinguishable peaks in the lipid head-tail interface. When increasing the hydrophobicity to $H = 0.8$, a trimodal distribution of NPs is clearly discernible in Figure3.3(red curves): a certain fraction of NPs are absorbed in the the core of the membrane, while others are located at the head-tail interface. Remarkable is that such a split up into three populations is still visible for $H = 1$, as shown in Figure3.3. It should be noted that the three-population structure of NPs represents a dynamic equilibrium, and that NPs were able to jump between these three different layers, i.e. upper leaflet, core of membrane and lower leaflet. This observation can also be found in the studies of the kinetic pathways (Sec.3.3.4), the potential of mean force (Sec.3.3.5) and the membrane perturbation (Sec.3.3.7). And it will be further discussed in a rather quantitative manner in the following sections.

Note that the observation that NPs prefer the layers in between the two leaflets has some similarities with the uptake/repulsion of NPs by polymer brushes [117–120]: The inclusion free energy of NPs increases with grafting density of polymer brushes, i.e. inserting NPs in the densely packed lipid bilayer requires higher free energy. High grafting density indicates a dense structure of polymer brush. In this case, the structure of leaflets of the self-assembled lipid bilayer is similar to polymer brushes. However, previous studies using the BFM [106] show that the distribution of NPs turned out to be homogeneous throughout the membrane profile. This difference emerges because the membrane, as modeled in the BFM, was less stiff, allowing NPs to distribute inside the leaflet.

3.3.2 NPs Translocation

The uptake of NPs can be controlled by the hydrophobicity as discussed above. In this section, the impact of hydrophobicity of NPs on the translocation rate is discussed. Here, a translocation event is defined if a NP translocates from the solvent phase on one side of the membrane to the solvent phase on the other side, passing through the core of the membrane (defined as the region $z = z_{center} \pm 15$ Å, with z_{center} being the center of mass of the lipid membrane). For a translocation event to be completed, the NP has to cross the boundaries defined as $z_{center} \pm 40$ Å. Note that the frequency of NP translocation across

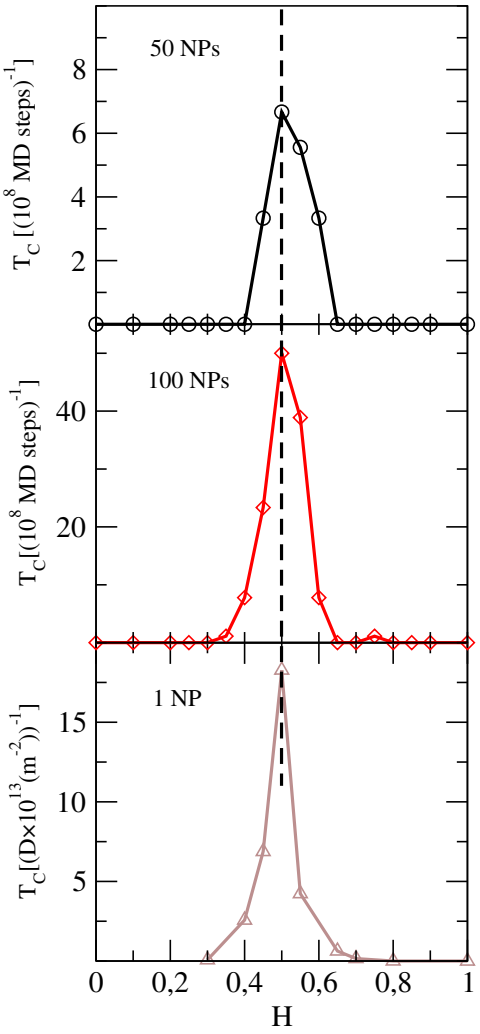

Figure 3.4: Translocation rates of NPs as a function of hydrophobicity, in the presence of 50 (black curve, circle symbols) and 100 NPs (red curve, diamond symbols). Brown line with triangle symbols present the results calculated from Kramers theory. Note that T_c in the last plot is in the scale of diffusion coefficient of NP (D). This figure is adopted from Ref. [111]

the bilayer is calculated as follows:

$$T_C = \frac{n_{NP}}{\Delta t}, \tag{3.5}$$

where n_{NP} is the number of translocation events of NPs across the bilayer during the simulation time Δt. The same method is used to calculate the translocation frequency of solvent beads.

Figure3.4shows that translocations of hydrophilic NPs with $H \leq 0.4$ and hydrophobic NPs with $H \geq 0.7$ were absent in our simulations, which is relevant to a considerable free energy barrier/trap shown in Figure3.8. At the hydrophobicity of $H = 0.5$, a maximum of membrane permeability for NPs occurs. The peak in the translocation rate is due to the role of the lipid membrane, which changes from a potential barrier to a potential trap. A further increase in hydrophobicity to $H = 1$ leads to a decrease of translocations of NPs though the lipid membrane. Note that translocation events in the presence of 100 NPs increase up to 10-folds when compared to 50 NPs, as shown in Figure3.4, indicating a cooperative effect when the concentration of NPs is sufficiently high. This cooperative effect is further discussed in the next section.

3.3.3 Concentration Effect of NPs

Translocation rate of NPs is governed by the hydrophobicity of NPs, as discussed above. In addition, the concentration of NPs plays an important role in the translocation. This is illustrated by the comparison between 50 and 100 NPs with balanced hydrophobicity ($H = 0.5$). As shown in Figure3.5, the membrane is destabilized where many particles are absorbed due to the filling-up of the states of the free energy minima (interfaces in this case). For the most interesting case, NPs with $H = 0.5$, both the solvent (water) and lipid core act as a poor solvent, *i.e.* a repulsive environment, which induces the formation of clusters of NPs for larger densities. Namely, particles can form bridges through the membrane at higher densities, thus forming gates for other particles. This phenomenon can be directly observed by considering the free energy landscapes for a given particle in the presence of 50 NPs and 100 NPs, respectively, see in Figure3.5. The free energy barrier for translocation becomes significantly flatter with increasing the number of NPs from 50 to 100. The cooperative effect can be reduced and even eliminated if the particles are patchy in terms of the hydrophobicity effect [106]. The bare interaction between the

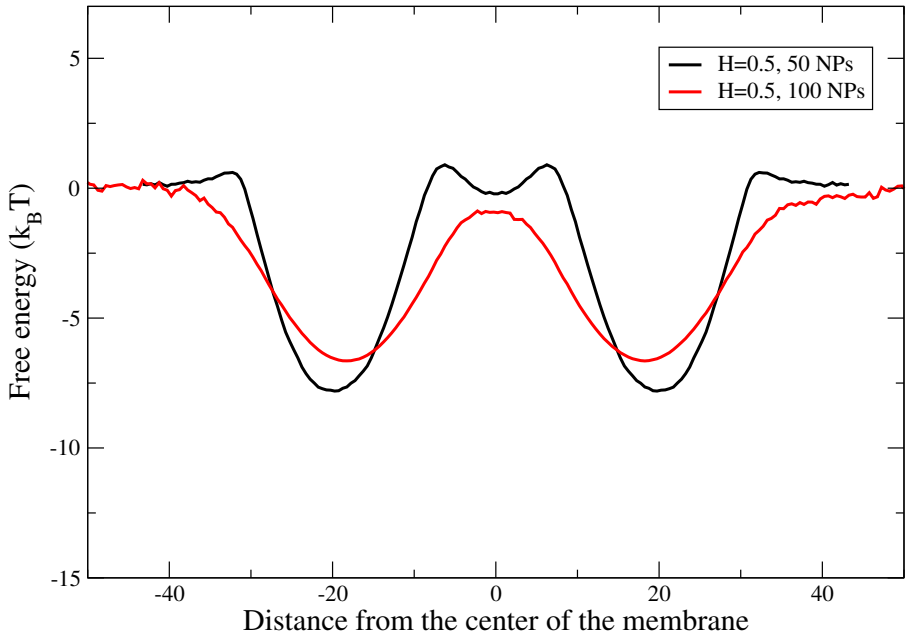

Figure 3.5: Free energy landscapes for a given NP in the presence of 50 and 100 NPs with hydrophobicity H=0.5. Here black and red lines present the cases of 50 and 100 NPs respectively.

NPs in this model is less important and the same effect can be observed if the particles have athermal pair interactions between each other for all values of the hydrophobiticy, see also Ref. [106].

To gain more insight in the cooperative effect, further simulations of systems in the presence of 70, 80, 90, 100, 110, 120, 130 and 140 NPs with balanced hydrophobicity, $H = 0.5$, interacting with the membranes were conducted. Figure3.6shows that the translocation rate of NPs increases dramatically when the number of NPs in the simulation box is larger than 70. Further simulations and studies are needed to completely examine the cooperative effect.

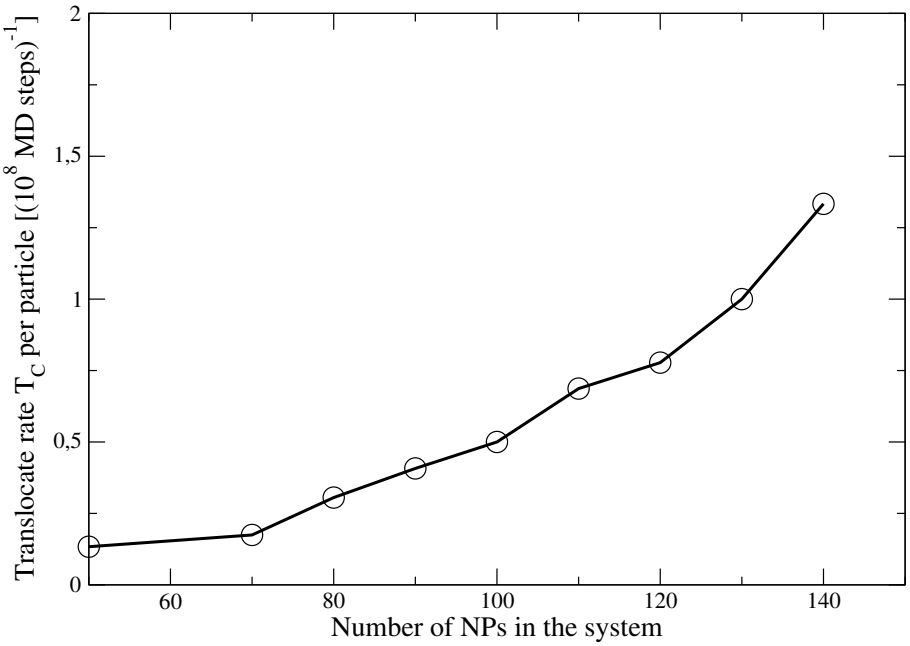

Figure 3.6: Translocation rate per NP as a function of the number of NPs in the simulation box.

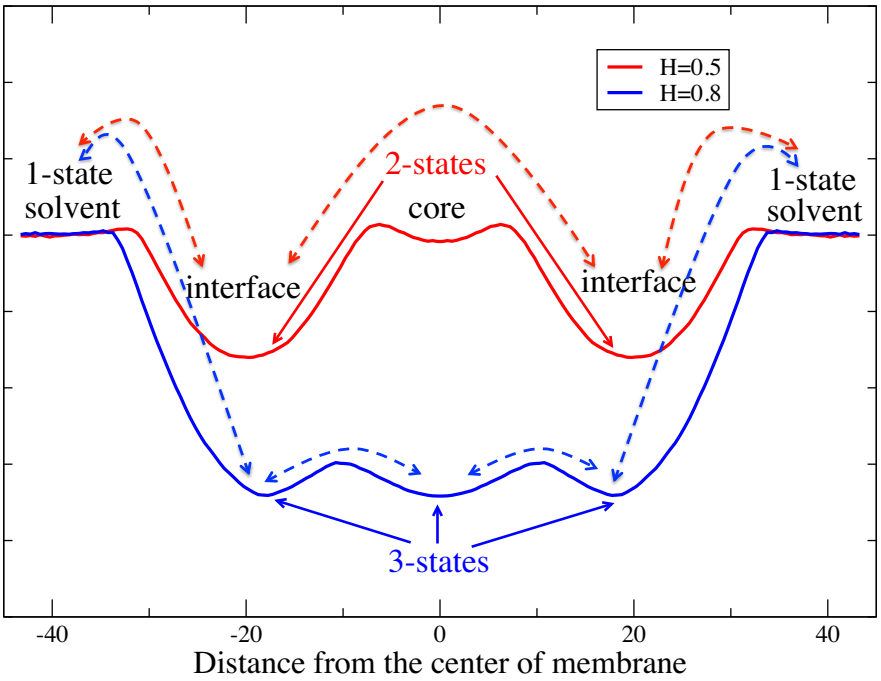

Figure 3.7: Sketch of the kinetic pathways of NPs with H=0.5 (red) and H=0.8 (blue) based on the analysis of the free energy landscape. The states of NPs are indicated as: solvent, interface, and core, i.e. between leaflets. The arrows indicate the rate of the processes.

3.3.4 The Effect of Hydrophobicity on Kinetic Pathways

The study of the distribution of NPs shows that at balanced hydrophobicity, $H = 0.5$, NPs locate at the lipid head-tail interface. And for partially hydrophobic NPs, $H = 0.8$, the distribution is not homogeneous, but displaying an effective three-populations pattern: NPs are dispersed in the lipid head-tail interface and in between the two lipid leaflets. Accordingly, with increasing hydrophobicity, for instance from $H = 0.5$ to $H = 0.8$, the positions of maximum NPs shift toward the core of the membrane. These findings lead to different kinetic pathways of translocation at different hydrophobicities as sketched in Figure3.7. For balanced hydrophobicity, at $H = 0.5$, the most interesting case, the NPs are mostly located at the membrane boundary where they can enter in the core of the membrane or leave for the solvent phase. This translocation pathway can be described by a 2+1-state process: to enter/leave the interface region from/to the solvated state;

to jump between the two interface states. This is indicated by the red double-headed arrows in Figure3.7. 2-states dominates the behavior inside the membrane, i.e. in the lipid head-tail interface. And 1-state corresponds to solvated state. The free energy barriers of detaching from the membrane and jumping between the two interface states are of the same order, see the free energy profile in Figure3.8. For higher hydrophobicities such as $H = 0.8$, a 3+1-state process becomes predominant where NPs jump between the interface regions and the inter-leaflet core positions. This is indicated by the blue double-headed arrows in Figure3.7. Note that “check-out" events become very rare and dominate the translocation time. The free energy barrier for leaving the membrane exceeds the order of 10 k_BT already for $H = 0.8$, see in Figure3.8. This indicates long translocation time, which is not accessible in the direct simulation.

It is worth noting that different kinetic pathways can be expected in the many NPs systems where collective effects play a role. As shown in Figure3.5, in the presence of 100 NPs, the free energy landscape for a individual particle becomes flatter (particularly at the interfaces) and bridging of the membrane by clustered particles can further facilitate the translocation process.

3.3.5 Potential of Mean Force

The general physical mechanism of passive translocation of particles through self-organized amphiphilic membranes could be depicted as passing through a free energy barrier. Therefore, it is of great importance to study the free energy profile of these systems. The theory of stochastic processes can be applied to calculate the mean first-escape time of NPs from the lipid bilayer, which might turn out to be much larger than the accessible simulation time.

The potential of mean force as a function of the distance of the NP from the center of the bilayer can be determined from the density profiles, $\rho(z)$, of the NPs:

$$F(z) = -k_BT \ln[\rho(z)] \; . \tag{3.6}$$

According to the definition, when the free energy differences are too high, the density of NPs is virtually zero during the simulation run. Whenever such a case emerges, umbrella sampling simulations were conducted as described in Sec.3.2. For instance, for hydrophobic NPs, umbrella sampling simulations were conducted in the region of the head-tail interface

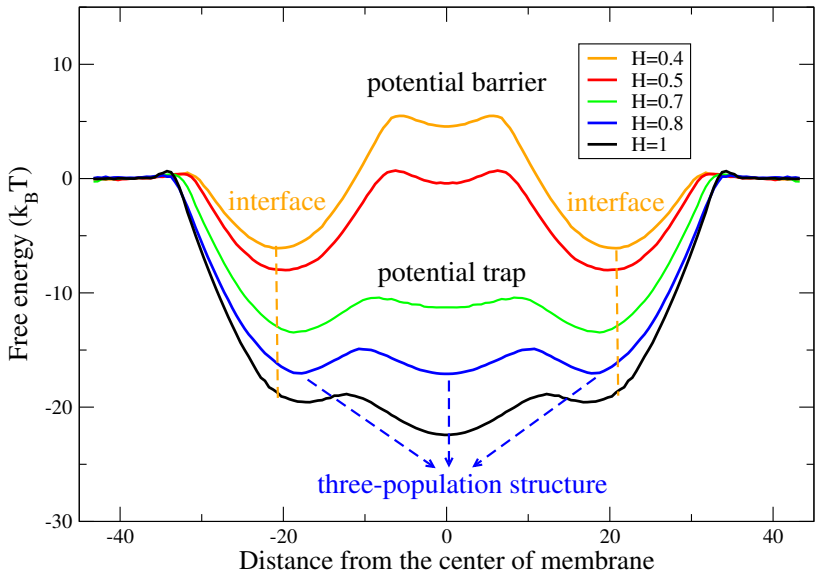

Figure 3.8: Free energy profiles as a function of the distance from the membrane centre, in the presence of 50 NPs, and at different hydrophobicities, H. The reaction coordinate denotes the distance of the NP from the center of mass-plane of the membrane. The lipid head-tail interface is indicated by the orange dash lines.

and in the solvent phase. Vice versa, umbrella sampling simulations were applied in the core of the membrane for hydrophilic NPs. Note that the free energy corresponds to the Gibbs free energy in our case, since the pressure is constant.

In this work, the potential of mean forces of NPs with different hydrophobicity are obtained from unbiased MD simulations of 50 NPs combined with umbrella sampling simulations of a NP. Here, all the free energy profiles are shifted to the reference (the solvent phase) with $F = 0$. Wherever the free energy is negative ($F(z) < 0$), NPs is absorbed and this region of the lipid bilayer represents a potential trap . Vice versa, $F(z) > 0$ corresponds to a potential barrier for NPs. For NPs with $H = 0.4$, the free energy profile first shows a potential trap in the interface, and a potential barrier in the core of the membrane. This indicates that NPs with $H = 0.4$ prefer the interface and the solvent phase. As shown in Figure3.8, with increasing the hydrophobicity of NPs from $H = 0.4$ to $H = 0.7$, the role of the bilayer is changing from a potential barrier to a potential trap. In the study of NPs' distribution, it is shown in Figure3.3that hydrophobic NPs form a three-

populations structure. Accordingly, the potential of mean force also reveals three energy minima, located in the two head-tail interfaces and between the leaflets. Note that a direct translocation of NPs with $H = 0.5$ across the membrane, as observed above, is related with an energy difference of 8 k_BT. Hydrophobic NPs ($H = 0.7, 0.8, 1$) are strongly absorbed inside the membrane. This can be quantitatively characterized by the free energy difference, which exceeds 10 k_BT corresponding to the fact that no translocation event is observed in the direct simulation.

With the potential of mean force shown in Figure3.8, the translocation rate of NPs through the lipid membrane can be studied by Kramers theory [121]. In this work, the translocation of NPs across the bilayer can be considered as a diffusive process over the energy barrier. And Kramers's method offers the solution for the mean first-passage time of the one-particle diffusion equation in a free energy landscape [122,123]:

$$\tau = \frac{1}{D} \int_{z_-}^{z_+} e^{F(z')/k_BT} dz' \int_{z_-}^{z'} e^{-F(z'')/k_BT} dz'' \tag{3.7}$$

Here, τ denotes the average time required for the diffusing particle to reach the layer z_+ on the trans-site of the membrane for the first time, if the particle was placed in the layer z_- on the cis-side of the membrane at the beginning. The location of z_+ and z_- has been chosen as $z_{center} \pm 40$ Å, which are the same thresholds used for direct calculation of the translocation rate and located well outside the membrane's profile, see also in Figure3.2. In this work, the diffusion coefficient D of the NPs is assumed to be constant along the direction perpendicular to the membrane (z coordinate). Precise measurements of passive translocation with the diffusion coefficient $D(z)$ as a function of z can be addressed in Ref. [114,124]. Corresponding results are shown in figure3.4(lower panel: brown line, triangle symbols). A pronounced peak of the membrane permeability for NPs is distinguishable at $H = 0.5$, which shows excellent agreement with observations of translocation events in direct simulations. The range of hydrophobicity ($0.4 \lesssim H \lesssim 0.7$) in which NPs can translocate through the bilayer is consistent with the direct simulations.

3.3.6 Hydrophobicity Scale

Essentially, a lipid membrane that consists of two packed layers of amphiphilic lipid molecules is driven by hydrophobic interaction. The hydrophobic effect is of great impor-

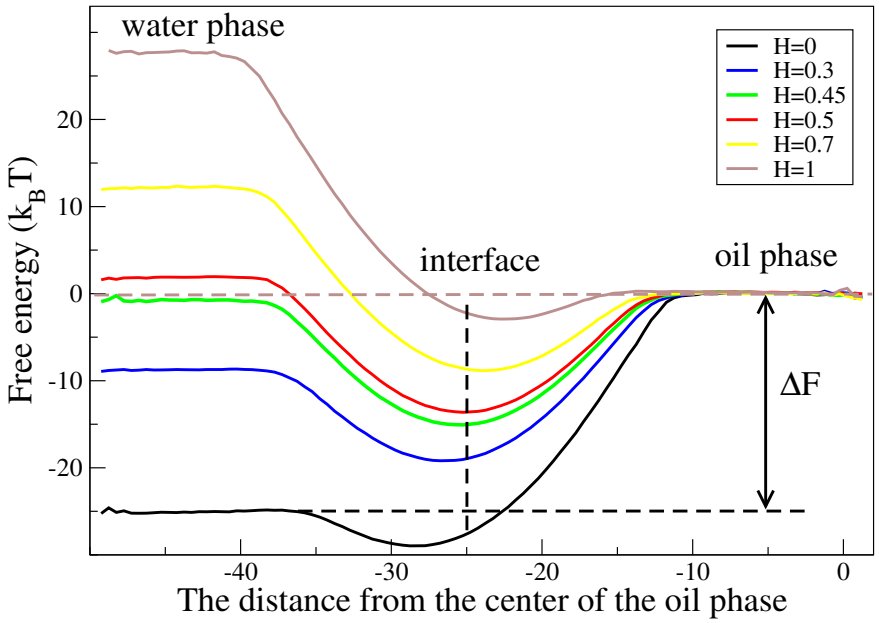

Figure 3.9: Free energy profiles of NPs as a function of the distance from the center of the oil phase. The location of the interface between the water and the oil phases is indicated as a dashed vertical line. Here, black, blue, green, red, yellow, brown lines denote $H = 0, 0.3, 0.45, 0.5, 0.7, 1$.

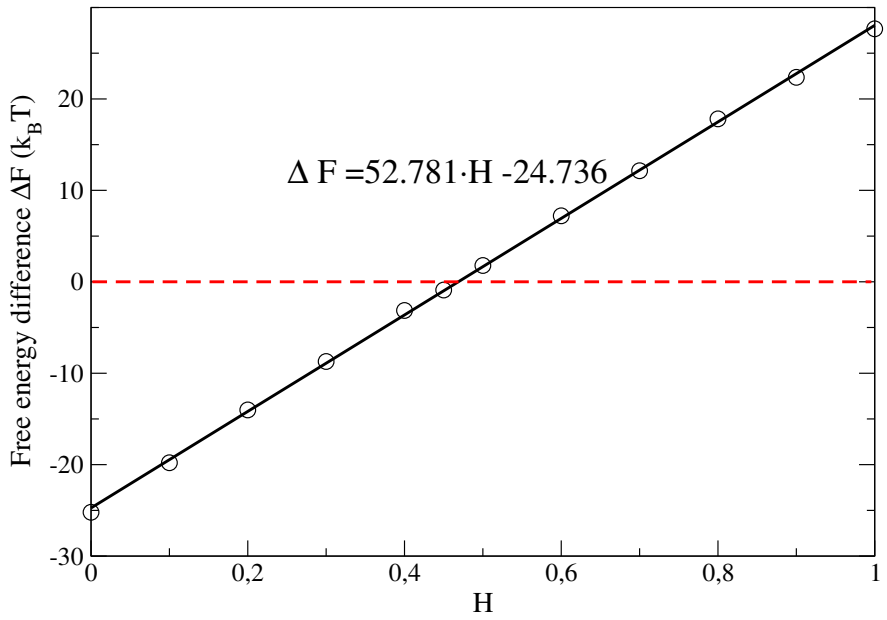

Figure 3.10: Hydrophobicity scale: Free energy difference between water and oil phases for NPs as a function of hydrophobicity H.

tance for the understanding of the interaction between the lipid membrane and NPs. The effective hydrophobic effect is a result of the interplay of all microscopic interactions which take place in the real system. Therefore, it is essential to map our microscopic model, characterized by the parameter H, to a hydrophobicity scale which is uniquely accessible in experiments.

Based on the principle of Radzicka Wolfenden partitioning scale for amino acid side-chains [125,126], MacCallum *et al.* conducted molecular simulations to calculate the free energy of partitioning between water and other regions of the membrane by the distribution of the side-chain analogs [127]. In this thesis, this hydrophobicity scale for NPs was conducted to quantify the hydrophobic effect by measuring the partition coefficient of NPs between the two phases: water and lipophilic solvent, the latter corresponding to a melt of oligomers (oil). This partition coefficient can be transferred to the free energy of

partitioning of NPs at the boundary between the two phases:

$$\frac{\Delta F}{k_B T} = \ln(K) = \ln(c_{\mathrm{H}}/c_{\mathrm{P}}). \tag{3.8}$$

Here, c_{H} and c_{P} in Eq.3.8denote the densities of NPs on the hydrophobic/hydrophilic side, respectively. And the partition coefficient is defined by $K = c_{\mathrm{H}}/c_{\mathrm{P}}$.

However, it is challenging to calculate the partitioning of NPs with a certain degree of hydrophobicity in oil and water phases in the direct MD simulations. For instance, it has extremely low frequency to observe fully hydrophilic NPs in the oil (non-preferable) phase during the direct simulations. In addition, partially hydrophilic/hydrophobic NPs are mostly located in the water-oil interface. Therefore, it is difficult to measure the partitioning of partially hydrophilic/hydrophobic NPs in water and oil phases. To address these issues, umbrella sampling simulations are conducted to calculate the free energy difference between water and oil phases for NPs of different hydrophobicities. Here, the reaction coordinate is chosen as the distance from the center of the oil phase in the direction perpendicular to the water/oil interface. The details of umbrella sampling simulations and the corresponding analysis by WHAM are the same as described in Sec.3.2, except that in these simulations the pressure allows for changes in the box size only in z-direction. Namely, the simulation box is fixed in the x and y coordinates. This is due to the fact that when the constant pressure condition is implemented in x and y directions, the interface between two phases is minimized since water beads and oil monomers tend to reduce the contact surface area with each other. The oil phase is composed of 1125 hydrophobic chains that are made of five tail monomers (5625 hydrophobic beads). And the water phase contains 5827 beads. In the initial configurations, hydrophobic chains and water monomers are separately dispersed in the upper and lower part of the box. A run of 30 ns (10^6 MD steps) was conducted for equilibration, followed by a production run of 600 ns ($2 * 10^7$ MD steps) in each sampling window.

Figure3.9shows the free energy profiles of NPs as a function of the reaction coordinate obtained from umbrella sampling simulations. These results show that for NPs close to the critical point of hydrophobicity ($H = 0.5$), the free energy difference between the phases vanishes, indicating that water and oil are indistinguishable for NPs. The free energy difference in the bulk of the two phases can be plotted as a function of the microscopic hydrophobicity H, see in Figure3.10. The simulation data can be fitted by the following

linear equation:

$$\frac{\Delta F}{k_B T} = 52.781 \cdot H - 24.736. \tag{3.9}$$

Since the free energy difference ΔF is directly related to the partitioning coefficient, this linear relationship can be used to map the parameter H to relevant experimental observations.

3.3.7 Solvent Permeation and Membrane Perturbation Induced by NPs

An interesting phenomenon addressed here is membrane perturbation induced by NPs of different degrees of hydrophobicity. Due to the interaction with NPs, the properties of the membrane change correspondingly, depending on the degree of hydrophobicity and concentration of the NPs, as shown in Figure3.11. Generally, in the presence of 100 NPs, a higher degree of membrane perturbation is observed. The upper panel of Figure3.11shows the membrane permeability for water *vs.* hydrophobicity of the NPs at two concentrations of NPs. Here, the membrane permeability in the presence of NPs is scaled with its solvent-permeability in the absence of NPs. The translocation event of solvent is counted with the same method as described in Sec.3.3.2. The boundaries of the translocation are chosen as $z_{center} \pm 30$ Å. It is shown that the permeability is generally increased whenever H differs from zero. Even in situations in which the NPs do not yet enter the membranes, they are capable of disturbing the molecular order of lipid and expanding the lipid bilayer, and thereby affecting the membrane permeability for water. In the presence of 100 NPs, a clear maximum of the permeability is visible at about $H = 0.7$. A similar observation is obtained in the study of amphiphilic NPs interacting with membranes [106], in which the amphiphilic NPs do not form any aggregation inside the membrane. Note that for $H = 1$ the permeability is slightly higher than for the case of $H = 0$. According to previous studies conducted with BFM [106], a stabilization effect, induced by hydrophobic NPs or hydrophobic polymers, led to an increase of the membrane thickness that, contrary to our results, reduced the permeability. In this study, the observed 4.5% increase of membrane thickness (2 Å) did not have any significant effect on the membrane's permeability with respect to solvent. By contrast, dynamic three-populations structure of hydrophobic NPs plays a role in the membrane perturbation. NPs move between these three layers: the core of the membrane and the two head-tail interfaces of the leaflets. This leads to a

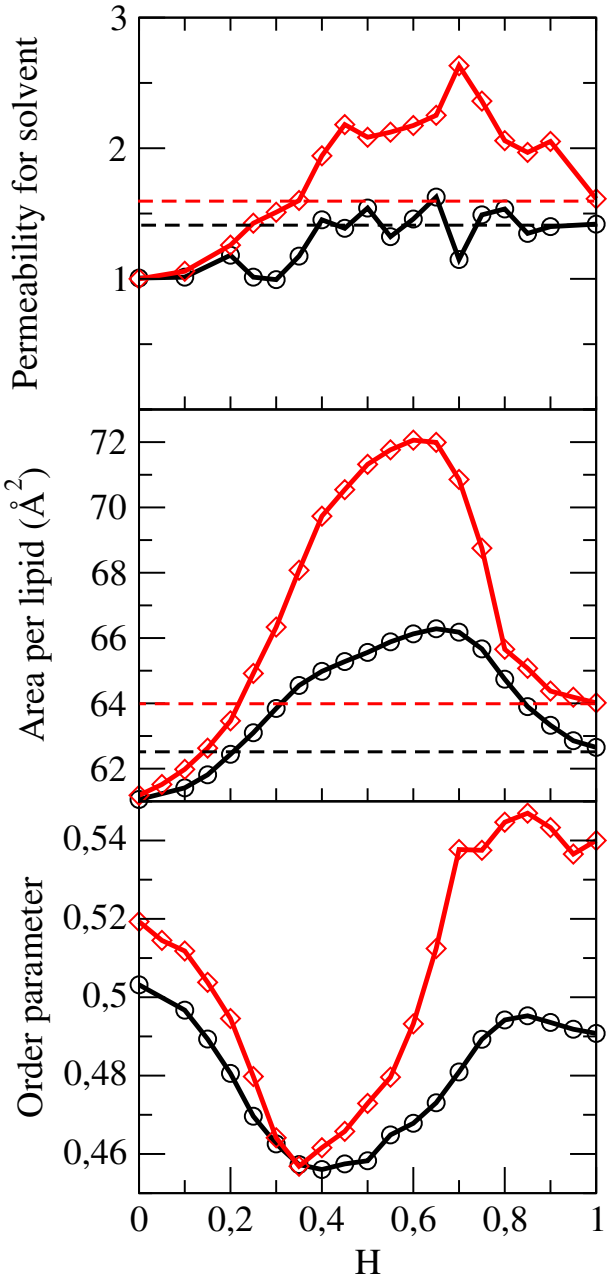

Figure 3.11: Relative membrane permeability for solvent (upper panel), area per lipid (center panel), and order parameter of lipid tails (lower panel), as a function of the hydrophobicity H, and in the presence of 50 (black curves, open circle) and 100 (red curves, open diamond) NPs.

considerable degree of membrane perturbation.

Another feature characterizing the state of the lipid bilayer is the area per lipid. The results highlight a correlation between the solvent permeability and the area per lipid, which is also presented in a recent review [124]. For $H = 0$, the area per lipid doesn't change compared with the pure lipid membrane system. With increasing hydrophobicity, NPs get absorbed by the lipid membrane. Once the dynamic three-populations structure of NPs is formed inside the membrane, NPs are pushing the lipid monomers away to occupy the space between these layers, which expands the lipid membrane to some extent. With a further increase of hydrophobicity of NPs, the majority of NPs stays put inside the core layer of the membrane, leading to weaker membrane perturbation induced by NPs, and a decrease of its area per lipid.

The order parameter of lipid tails was calculated to quantify the tail orientation and the effect of hydrophobicity on the structural properties of the bilayer. The definition of the order parameter P_2 is introduced in Chapter1. The corresponding results are displayed in the lower panel of Figure3.11. A minimum of the orientational order parameter close to $H = 0.5$ is visible, indicating a maximum of membrane perturbation induced by NPs. This is correlated with the fact that around $H = 0.5$ NPs frequently penetrate in and detach from the membrane. Note that wrapping behavior of bilayers induced by NPs is not observed in the simulations. Therefore, the change of order parameter is only related to membrane disruption, rather than membrane curvatures.

3.4 Summary

In this work, a simplified version of the MARTINI model is implemented to systematically investigate lipid bilayers interacting with NPs of various hydrophobicity on coarse-grained level. The results demonstrate that the hydrophobic of NPs governs the uptake. Hydrophilic NPs get repelled from the core of the membrane, vice versa, hydrophobic NPs are absorbed by the bilayer. At intermediate hydrophobicity, for instance $H = 0.8$, the distribution of NPs inside the membrane displays an effective three-populations pattern: NPs are preferentially located in the regions between the head and tail groups, and in between the leaflets of the two lipid layers. The preference for the location between the leaflets is enhanced with increasing hydrophobicity.

Furthermore, the distributions of NPs under various hydrophobicities lead to different kinetic pathways of translocation. For balanced hydrophobicity, at $H = 0.5$, NPs disperse in the lipid head-tail interface of the two leaflets. The corresponding translocation pathway is basically entering/leaving the interface region from/to the solvated state, and jumping between the two interfacial states. For higher hydrophobicities such as $H = 0.8$, NPs jump between the interface regions and the inter-leaflet core positions. Detachment from the bilayer becomes very rare and dominates the translocation time. In addition, different kinetic pathway of translocation is expected when cooperative effects play a role. Regarding translocation rates of 100 and 50 NPs, a cooperative effect is observed. In the presence of many NPs, they can form bridges through the membrane in the interface, thus forming gates for other NPs to translocate across the membrane. This phenomenon can be directly verified by the flatter free energy landscape for a given particle in the presence of 100 NPs.

The general physical mechanism of passive translocation of NPs through self-organized amphiphilic membranes can be depicted either as potential traps or potential barriers with respect to NPs, depending on their hydrophobicity. This is verified by the study of the potential of mean force. Using these free energy profiles, the mean first-passage time of a diffusing particle in the free energy landscapes can be calculated by Kramers theory. Results obtained from Kramers theory are consistent with the findings from direct simulations, display a narrow window of high translocation rates for NPs with a balanced hydrophobicity close to $H = 0.5$, thus verify the potential model of the lipid membrane. At this point the free energy landscape is maximally flat and the remaining barrier can be associated with the entropy reduction of the tails by accommodating the particle.

In order to relate the microscopic definition of hydrophobicity of NPs to experiments, which is based on the CG interaction model, a series of simulations of a water/oil system is conducted and the free energy difference of the NP distributed in the water and oil phases is further calculated from the partition coefficient. At the balanced hydrophobicity, H=0.5, either oil monomers or water beads are identical for NPs. Namely, for NPs, the free energy difference between oil/water phases vanishes. This corresponds to the finding of the potential of mean force, *i.e.* the maximally flat free energy profile for NPs with $H = 0.5$. The free energy difference of the NP between the two phases can be further plotted as a function of the microscopic parameter H. The results demonstrate a linear relation, allowing for a direct mapping of simulation results with experimental observations.

The uptake of NPs influences the properties of the lipid bilayer. Partially hydrophobic

NPs ($0 < H < 1$) enhance the membrane permeability for water considerably, expand the lipid membrane and disturb the order of lipids. Particularly, at the intermediated hydrophobicity, dynamic three-populations structure can further enhance the membrane perturbation. Additionally, simulation results imply a correlation between the area per lipid and the NP-induced permeability of the membrane. These effects are not related to any pore formation of the membrane or membrane curvatures, but rather a consequence of the fact that the lipid layer is a self-organized liquid state representing a free-energy barrier/landscape for NPs.

4 Coarse-grained Model of Oxidized Lipids and their Interactions with NPs of Varying Hydrophobicities

4.1 Introduction

When membranes are exposed to oxidative stress, they are susceptible to oxidative attack due to the high amount of targets such as proteins, monounsaturated and polyunsaturated acyl chains [128,129]. Moreover, the oxidation of the membrane is supported by the fact that interactions with oxygen are more favorable in the hydrophobic region of the lipid bilayers, rather than in the solution [130]. Hydroperoxidized chains result from the interaction of unsaturated double bonds in the alkyl chains with singlet oxygen produced when dye molecules (fluorophores or photosensitizers) are illuminated [131]. Hydroperoxidized lipids are in particular created during the phototherapy treatments of some tumors, and their precise role in the process is currently investigated both theoretically and experimentally.

Membrane fluidity is of great importance in biological processes, and mainly determined by the phospholipids. Even minor changes on membrane fluidity can affect the function of the membrane such as membrane fusion and induced pathology. Recent studies show that the membrane fluidity decreases upon oxidation [132]. It is also reported that the local lipid mobility and lateral diffusion of oxidized phospholipids in single unilamellar vesicles are reduced due to the oxidation effect [11]. Moreover, oxidized lipids can also disturb the conformation of the bilayer. For instance, oxidized lipids can induce phase separations in the densely packed DPPC-rich membrane, but have no influence on the linoleoyl-palmitoyl-lecithin (LPPC)-rich membrane [13]. Studies on isolated mitochondria show that the lipid oxidation can destroy the lipid bilayer packing in vitro [14] and in vivo [15].

Although oxidation products can damage the membrane and induce a loss of the membrane's function as a barrier [18,19,133], these phenomena can in turn be beneficial to medical treatment against infection and the selective killing of bacteria. Reactive oxygen species (ROS) are chemically reactive molecules, which play important roles in cell signaling and homeostasis [134]. A high level of ROS leads to a damage in the lipids, proteins and DNA. However, a certain amount of ROS can promote cell proliferation and control the function of the cell. Manipulating the amount of ROS in the cell can selectively kill tumor/cancer cells without causing significant damage to the normal cell [135–137]. The potential uses of ROS to selectively kill bacteria is also reported [138].

Due to the fact that oxidation products can alter the properties of lipid bilayers, including the stability, fluidity, elasticity and permeability, oxidized membranes have attracted attention from the fields of biology, biochemistry, pharmacy and food sciences. Nevertheless, it still remains an open question what the roles and mechanisms of oxidation products are. Specifically, how oxidation products affect the membrane permeability and selectivities, and how NPs can interact with the oxidized lipid bilayer. Further informations in terms of NPs translocation through oxidized bilayers and NPs' toxicity to the oxidized bilayers are still missing. To answer these questions, two types of oxidized lipid bilayers are characterized, followed by the study of the oxidation effect on the interaction between oxidized bilayers and NPs. In this Chapter, CG models used to construct oxidized lipid membranes are described in Sec.4.2. The structural and elastic properties of oxidized bilayers are further characterized in Sec.4.3.1. Then oxidized lipid membranes interacting with NPs of various degrees of hydrophobicity are studied in Sec.4.3.2, *i.e.* the uptake of NPs in the oxidized membranes, NPs translocation through oxidized bilayers, membrane perturbation induced by NPs and membrane permeability for solvent. The discussions and findings are summarized in Sec.4.4.

4.2 Coarse-grained Model and Simulation Details

In this Chapter, we focus on one special class of compounds: the hydroperoxidised lipid chains, where a peroxide group -OOH is attached to a carbon at the vicinity of the unsaturated double bond C=C. In what follows, the term oxidized lipid refer exclusively to this kind of hydroperoxidised chain. An extension of the modified MARTINI model [37], described in Chapter3, is implemented to construct oxidized lipid bilayers interacting

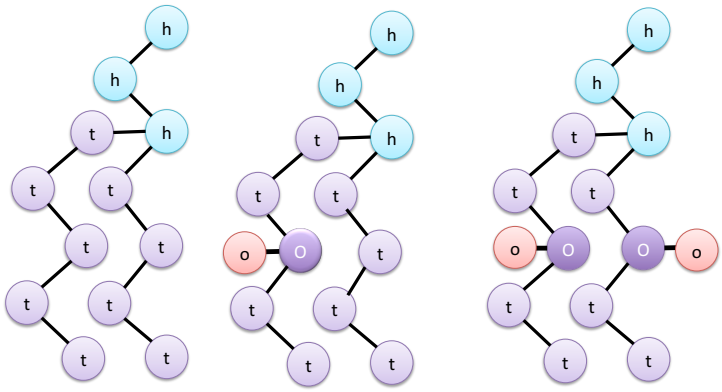

Figure 4.1: Scheme of the coarse-grained models for non-oxidized lipid, oxidized lipid oxidized with one tail and two tails. Here, h, t, O, o represent the lipid head, tail, hydrophobic and hydrophilic oxidized beads.

with NPs. In the MARTINI model, each non-oxidized group C_4 forming the lipid tail is represented by a hydrophobic bead with a standard size of 4.7Å. To reproduce the polar character of oxidized group C_4OOH that is larger than the original non-oxidized group C_4, a set of hydrophobic beads (representing C_4) with standard size of 4.7 Å and hydrophilic beads (representing -OOH group) of 4.7 Å is introduced, as shown in Figure4.1, where hydrophobic oxidized beads are labeled with O and hydrophilic oxidized beads with o. The adjunction of a hydrophobic oxidized bead to a hydrophilic oxidized bead is chosen to be 3.2 Å, which is shorter than other bond lengths and was suggested by Thalmann and Guo *et al.* [139], according to systematic investigations and comparisons with experimental studies of hydroperoxidation of 1-palmitoyl-2-oleoyl-sn-glycero-3-phosphocholine (POPC) and 1,2-dioleoyl-sn-glycero-3-phosphocholine (DOPC) bilayers [140] and vesicles [141].

The force field implemented in this work (as described in Chapter3), contains a Lennard-Jones (LJ) pair-potential, a bonding potential and an angle potential. Note that the angle potential between oxidized beads and connected tail monomers is excluded. Lipid head monomers, solvent beads and hydrophilic oxidized beads are identical in terms of hydrophobic interactions. Moreover, hydrophobic oxidized beads and tail groups are equal in our model. The strategy for mediating effective interaction potentials between NPs of

varying hydrophobicities and other components is the same as discussed in Chapter3.

Due to the presence of two different forms of oxidation, two types of oxidized lipids are considered: those oxidized with one and two tails, as shown in Figure4.1. Here, oxidized lipid membranes composed of lipids that are oxidized with one tail and two tails are denoted as OX1 and OX2, respectively.

The simulations were conducted with the open source LAMMPS molecular dynamics package [115] using highly parallelized code. The systems were run in NPT ensembles with time steps of 30 fs, at constant temperature (323 K, damping parameter 3000 fs) with pressure coupled to a MTTK barostat (1 bar, damping parameter 30000 fs). Periodic boundary conditions were implemented in all directions. For the initial configuration, 450 oxidized lipid molecules have been arranged into two bilayer leaflets in the cubic simulation box of size 135 Å, while solvent beads and NPs were dispersed outside the lipid membrane. A relaxation of 300 ns (10^7 MD steps) was carried out. It was followed by a production run of 2700 ns ($9 * 10^7$ MD steps), during which a trajectory of 90000 configurations was stored for data analysis.

4.3 Results and Discussions

4.3.1 Characterizing the Oxidized Lipid Membranes

Structural and Elastic Properties of Oxidized Bilayers upon Oxidation

The introduction of hydrophilic oxidized beads in the lipid tails leads to dramatic changes in the properties of the membrane. Due to the hydrophilic nature of oxidized beads (-OOH), they show a strong affinity for lipid head groups. As a consequence, oxidized lipid tails tend to bend towards the hydrophilic phase. This readily explains the expansion of oxidized lipid membranes, *i.e.* the area per lipid increases significantly upon oxidation as shown in Figure4.2. For instance, for oxidized lipid membranes OX1 and OX2, the area per lipid increases to 74.25 $Å^2$ and 76.30 $Å^2$, respectively. Such an increase obtained in our simulations is comparable to recent studies from the perspectives of experiments [140, 141] and MD simulations [139] of DOPC, POPC bilayers and vesicles. Note that such an increase of the area per lipid is accompanied by a decrease of the bilayer thickness to 39.5 Å for oxidized membranes both OX1 and OX2. Moreover, the order parameters of lipid tails

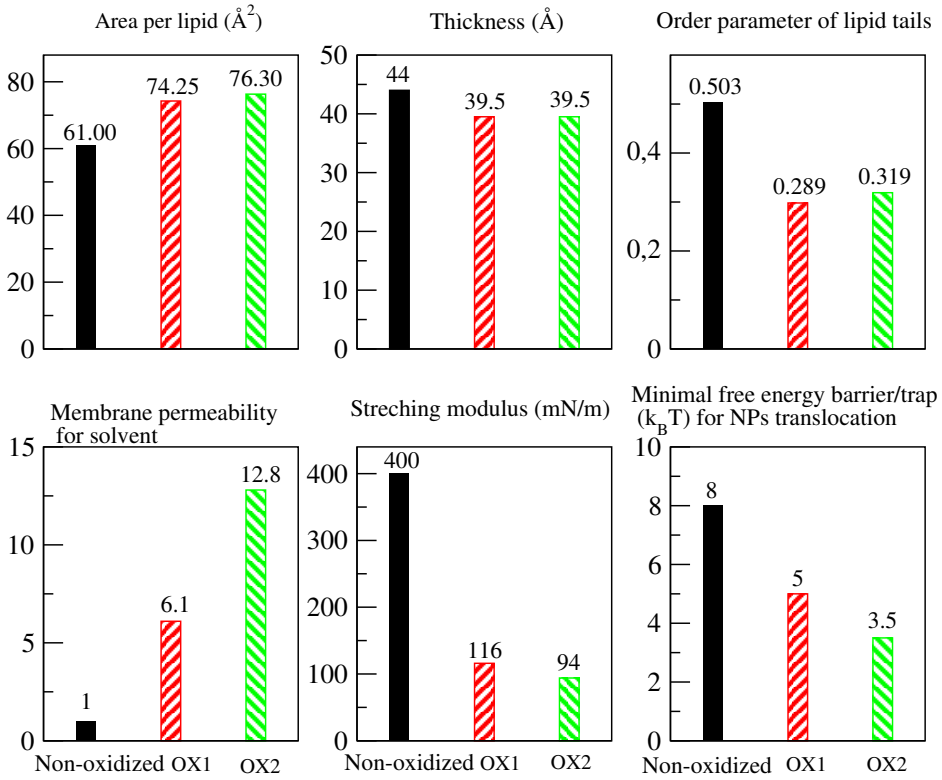

Figure 4.2: Comparisons of properties of non-oxidized bilayers as obtained in Chapter3 and oxidized bilayers as obtained in the present chapter.

of OX1 and OX2 decrease to 0.289 and 0.319, respectively, which are lower than the case of non-oxidized bilayer (0.503). It is worth noting that the behaviors of oxidized lipid membranes OX1 and OX2 are qualitatively similar. Oxidation upon both tails does not trigger a significantly higher expansion of the surface area. This is due to the limited space in the head-tail interfacial region in which only a certain mount of hydrophilic oxidized beads can be accommodated. Therefore, the extra hydrophilic oxidized beads disperse in two leaflets of bilayers and do not further contribute to the surface expansion. We will return back to this point in the discussion of the distribution of oxidized beads as shown in Figure4.3.

Another significant effect induced by oxidation is that water permeation through the membrane becomes feasible. The membrane permeability for water is calculated according to Eq.3.5. In the comparison to non-oxidized bilayer, the membrane permeability for solvent is scaled with the area of the bilayer to exclude the size effect of the bilayer. Figure4.2shows that membrane permeability for water of oxidized membranes OX1 and OX2 increases to 6.1-folds and 12.8-folds, respectively. This is due to the increased distance

between lipids as a result of the preference of hydrophilic oxidized beads to reside in the hydrophilic region of the bilayer. Note that the remarkable enhanced water penetrating through the bilayers is not related to any hole damage, but rather the consequence of expansion of surface area. Similar effect was observed in recent studies: the permeation of water is increased by one or two orders of magnitude when compared to non-oxidized membranes [16,17].

The elastic properties of oxidized membranes are examined by studying the stretching modulus K_A that is extracted from an area fluctuation analysis as followed:

$$K_A = \frac{k_B T \langle A \rangle}{\langle A^2 \rangle - \langle A \rangle^2} = \frac{k_B T}{4(\langle L_x^2 \rangle - \langle L_x \rangle^2)}, \tag{4.1}$$

where $A = L_x L_y$ is the area of the lipid bilayer and L_x is the lateral size of the simulation box. Since the barostat is coupled in x and y direction, L_x equals to L_y. The results in Figure4.2show that the stretching modulus of the oxidized membranes OX1 and OX2 drops to 116 and 94 mN $\cdot$ m^{-1}, respectively. Such a sharp drop of stretching modulus of oxidized bilayers is consistent with previous studies [139].

Distributions of Different Species in Oxidized Bilayers

Figure4.3depicts distributions of different species in non-oxidized and oxidized bilayers. It should be noted that for oxidized bilayers OX1 and OX2 a certain amount of hydrophilic oxidized beads is observed even in between the two leaflets of oxidized bilayers. It is also found that hydrophilic head groups penetrate more deeply even into the core of the membrane upon oxidation, as a result of a certain amount of tilting lipids. Figure4.3 shows that the main difference between the oxidized lipid membranes OX1 and OX2 is the distribution of hydrophilic oxidized beads. For the oxidized membrane OX1, hydrophilic oxidized beads prefer to locate not only in the lipid head-tail interface but also in the core of the membrane (green line in the middle panel of Figure4.3). By contrast, for oxidized membrane OX2, oxidized with two tails, the majority of hydrophilic oxidized beads disperses in the leaflets. Due to the symmetric structure of lipids oxidized with two tails, they are less prone to tilt. This is consistent with the findings of distribution of tilting angles as discussed below. Additionally, due to the limited space in the interfacial region, extra hydrophilic oxidized beads disperse in the leaflets.

Additional information about the conformation of oxidized lipid is found in the distribution

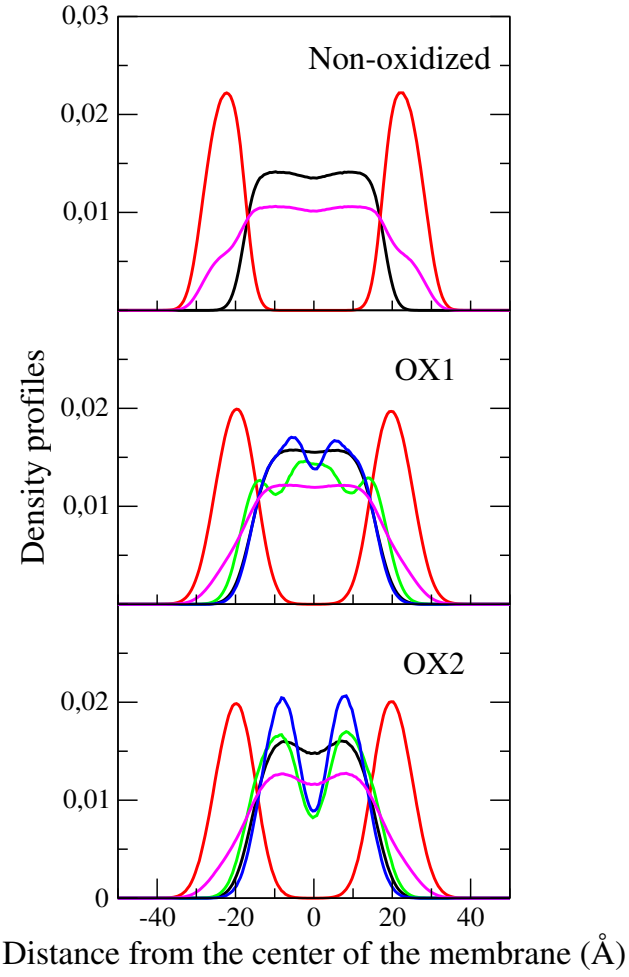

Figure 4.3: Density profiles of different species of non-oxidized bilayer (upper panel), lipid membranes oxidized with one tail (middle panel: OX1) and both tails (lower panel: OX2). Head group (red lines), tail group (black lines), hydrophobic oxidized group (blue lines), hydrophilic oxidized group (green lines), total density of lipid molecules (magenta lines) are presented as a function of distance from the center plane of the membrane, z.

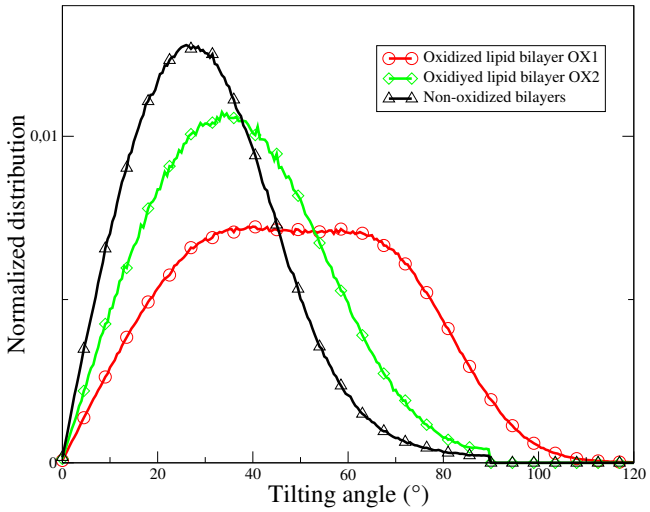

Figure 4.4: The distribution of tilting angles of lipids for the non-oxidized bilayer (black line), the oxidized bilayers OX1 (red line) and OX2 (green line).

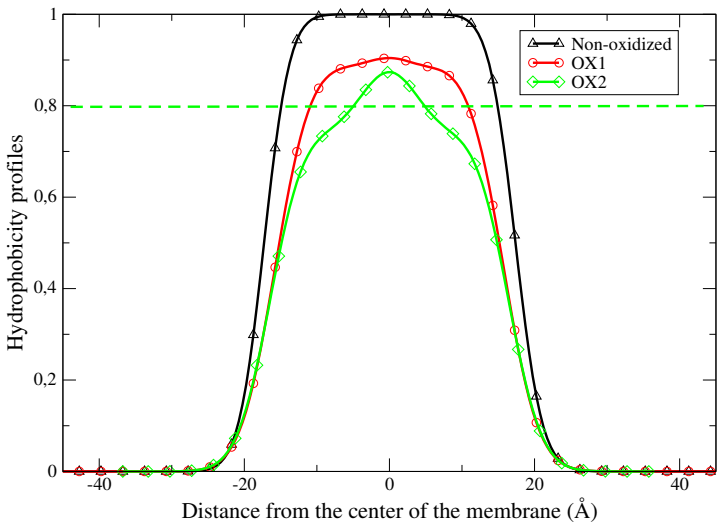

Figure 4.5: Hydrophobicity profiles of the non-oxidized bilayer (black line), oxidized bilayers OX1 (red line) and OX2 (green solid line). Here, the green dashed line denotes the average hydrophobicity of the core of the oxidized bilayer OX2. The core region is defined as the region between $z = z_{center} \pm 10$ Å, with z_{center} being the center of mass of the lipid membrane.

of tilting angles as shown in Figure4.4. The tilting angle is defined as the angle between the oxidized tail and the direction normal to the membrane (z axis). For oxidized bilayer OX1, it depicts a higher occupation in the high tilting angle region, indicating that lipids tend to tilt. However, for the oxidized bilayer OX2, the distribution of tilting angles is narrow, and displays a peak value around 34°, slightly higher compared to the non-oxidized bilayer (27°). When lipids are oxidized with only one tail, the symmetry of lipid conformation breaks down, driven by the attractive interaction between hydrophilic oxidized beads and the lipid head group. As a consequence, lipids oxidized with one tail show a higher tendency to tilt.

Furthermore, hydrophobicity profiles of the bilayers are illustrated in Figure4.5. The hydrophobicity profiles are calculated by averaging the hydrophobicity of beads located at the same plane perpendicular to the membrane. Upon oxidation, a drop of 10% and 20% of the average hydrophobicity H in the core of the oxidized bilayers is observed for the oxidized bilayer OX1 and OX2, respectively. The core of oxidized bilayer OX2 ($H = 0.8$) is more hydrophilic than OX1 ($H = 0.9$) due to the fact that more hydrophilic oxidized monomers disperse in the bilayers. This point is highly relevant for the discussion of NP translocation through the bilayers, as described below.

4.3.2 Oxidized Lipid Membranes Interacting with NPs of Various Degrees of Hydrophobicity

As discussed in Sec.4.3.1, oxidation effect on the lipid tails induces significant changes on the membranes, i.e. the area per lipid increases, with subsequent decrease of membrane thickness; the stretching modulus of oxidized membranes drops; whereas membrane permeability for water increases dramatically. The question then arises on how the interplay between NPs and oxidized bilayers changes. Figure4.6shows the distributions of NPs in the oxidized membranes OX1 and OX2. It is observed that both OX1 and OX2 oxidized membranes change from potential barriers to traps for NPs with increasing hydrophobicity from $H = 0$ to $H = 1$. This is consistent with the function of non-oxidized bilayers. It may be noted that a trimodal distribution of hydrophobic NPs is less pronounced, compared with the studies of non-oxidized lipid membranes presented in Chapter3. However, it exists in a narrow window of hydrophobicity (data not shown for other hydrophobicities). For the distribution of hydrophobic NPs ($H = 1$), the partition into three populations diminishes, i.e. the “shoulder" of the hydrophobic NPs distribution at the head-tail interface vanishes. This can be understood by the fact that the oxidized membranes become softer

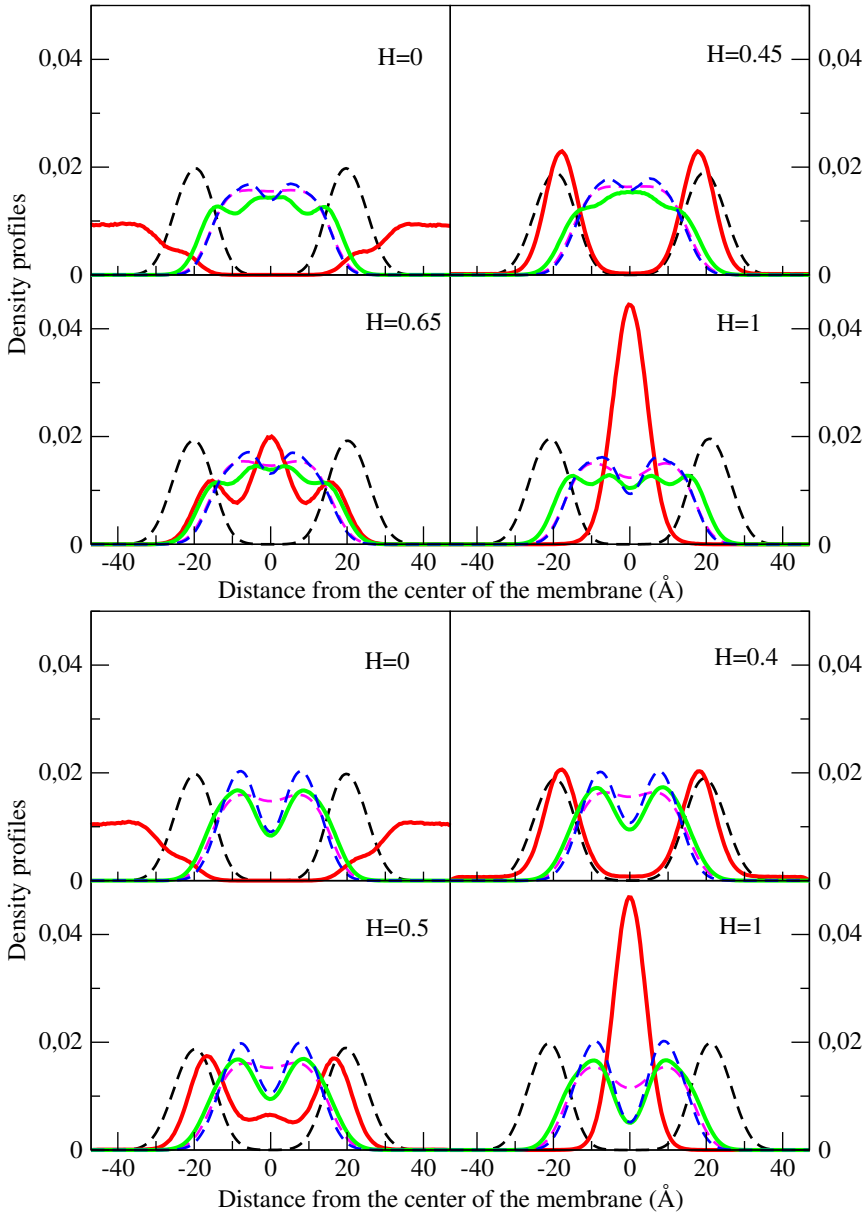

Figure 4.6: Density profiles of different species of oxidized bilayers OX1 (upper panel) and OX2 (lower panel) in the presence of 50 NPs of different hydrophobicity. Head group (black/dashed lines), tail group (magenta/dashed lines), hydrophobic oxidized group (blue/dashed lines), hydrophilic oxidized group (green/solid lines) and NPs (red/solid lines) are presented as a function of distance from the central plane of the membrane, z. The four different plots in the figure correspond to different levels of hydrophobicity, as indicated inside the plots.

and looser upon oxidation, allowing hydrophobic NPs to disperse in the leaflet of oxidized membranes. Note that this absence of three-populations structure for hydrophobic NPs in the oxidized bilayers is coherent with the previous studies by BFM [106]. Another phenomenon addressed is that hydrophilic oxidized beads in the oxidized bilayer OX1 accommodate to the uptake of NPs, i.e. adjusting their distribution according to the preference location of NPs inside the membrane when increasing the hydrophobicity of NPs.

NPs Translocate through Oxidized Lipid Membrane: a Study of the Potential of Mean Force

Figure4.7shows the translocation rates of NPs as a function of their hydrophobicity, as obtained from MD simulations. The pronounced peaks of NP translocation through oxidized bilayers OX1 and OX2 are located at $H = 0.45$ and $H = 0.4$, respectively. This indicates that the critical point for NP translocation shifts into a region of lower hydrophobicity, compared with the non-oxidized bilayer ($H = 0.5$). These shifts are related to the same decrease in the percentage of average hydrophobicity in the core of the bilayers upon oxidation (see Figure4.5). Another interesting observation is that for oxidized bilayers the maximum translocation rate of NP at the critical hydrophobicity increases significantly compared with the case of the non-oxidized membrane. This is triggered by the fact that oxidized bilayers tend to be softer and looser upon oxidation, accompanied with an increase of the surface area as a result of hydrophilic oxidized beads being adjacent to the tail. These findings can be verified by the following studies of the potential of mean force presented in Figure4.8.

For oxidized bilayers interacting with NPs at the critical hydrophobicity, we can directly obtain the potential of mean force from the density distribution of NPs: $F(z) = -k_B T \ln(\rho(z))$. This yields a lowest free energy difference of about 5 $k_B T$ for NPs with $H = 0.45$ during a translocation through the oxidized bilayer OX1 (left panel of Figure4.8), and 3.5 $k_B T$ at $H = 0.4$ for the oxidized bilayer OX2 (right panel of Figure4.8). This finding is also summarized in Figure4.2. Compared with the non-oxidized membrane, the oxidized membrane acts as a lower free energy barrier for NPs translocating through the bilayer. As a consequence, translocation rates of NPs through oxidized membranes increase significantly, which provides a possible mechanism for NPs translocating through biological membranes by the benefit of oxidation effects.

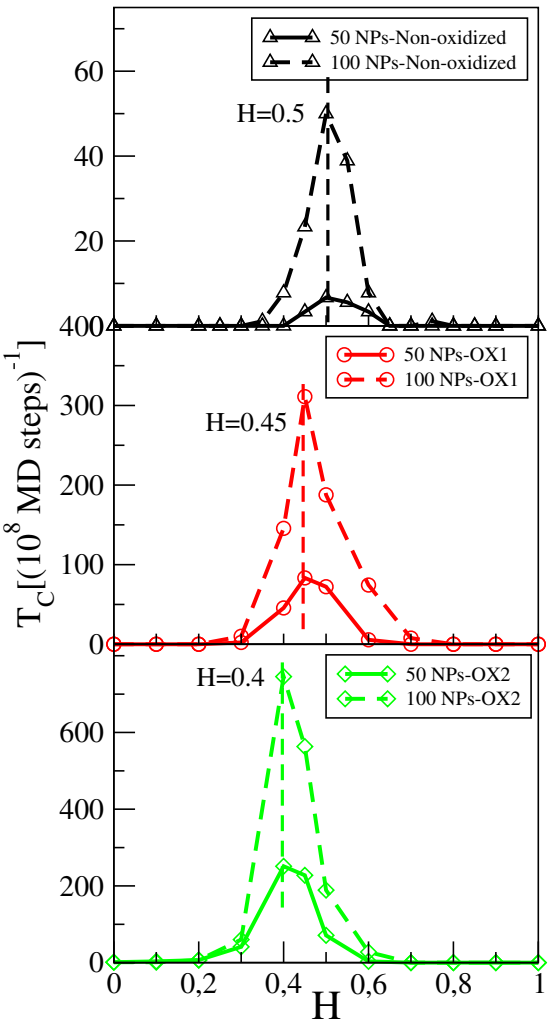

Figure 4.7: Frequency of translocations of NPs through non-oxidized bilayer (upper panel), oxidized bilayers OX1 (middle panel) and OX2 (lower panel) as a function of hydrophobicity, in the presence of 50 and 100 NPs. Here, solid lines and dash lines denote the cases of 50 and 100 NPs, respectively.

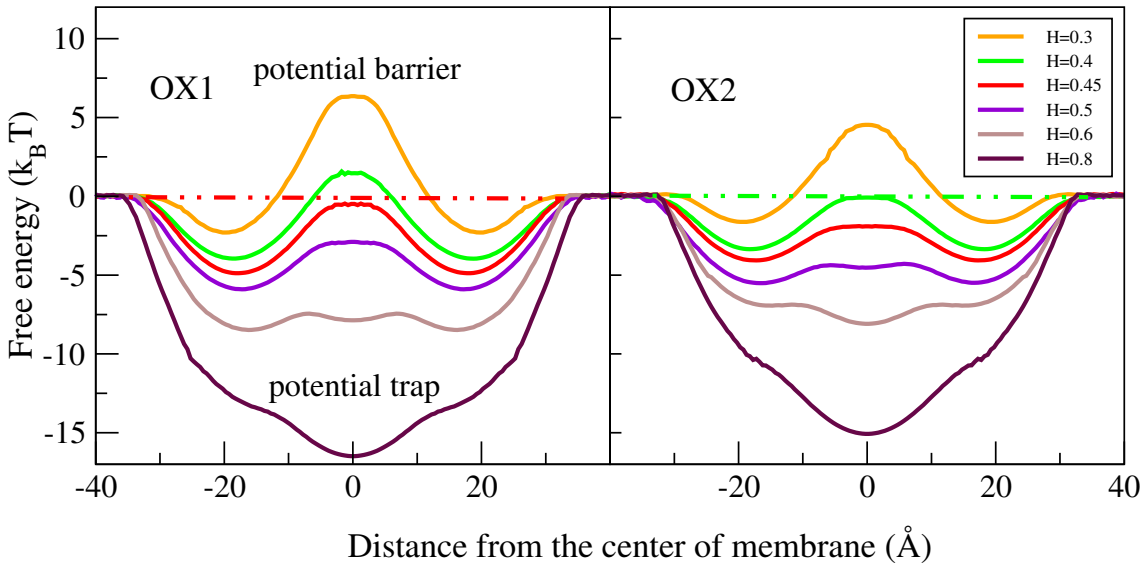

Figure 4.8: The free energy profiles for NPs of different hydrophobicities translocation through the oxidized lipid membrane OX1 (left panel) and OX2 (right panel). Here, the lipid bilayer is perpendicular to the z coordinate.

For more hydrophilic/hydrophobic NPs, it is infeasible to obtain sufficient samples for all coordinates from direct MD simulations. Therefore, umbrella sampling simulations are conducted whenever the statistics obtained from direct sampling is not sufficient. Then, the umbrella sampling results are combined with the direct MD simulation results in order to obtain the free energy profile over the entire range. Details of umbrella sampling simulations are described in Chapter2and Chapter3. As shown in Figure4.8, oxidized bilayers of both OX1 and OX2 change from potential barriers to potential traps when increasing NPs' hydrophobicity. For NPs at the critical hydrophobicity ($H = 0.45$ for OX1, $H = 0.4$ for OX2), the free energy profiles are essentially flat. This corresponds to the observation of maximal NP translocation rates as obtained from direct MD simulations (see Figure4.7). Note that the free energy profiles for NPs during a translocation through the oxidized bilayer OX1 and OX2 are similar, though the oxidized bilayer OX1 presents a slightly flatter and narrower barrier/trap.

With these free energy profiles, we further calculate the mean first-passage time τ by applying the Kramers theory (as described in Chapter3), for a single NP passive translocation through the oxidized bilayers OX1 and OX2. The translocation rate T_C can further be calculated from the inverse of the mean first-passage time τ. As shown in Figure4.9, the results of the translocation rate T_C coincide with the direct MD simulations: a pronounced

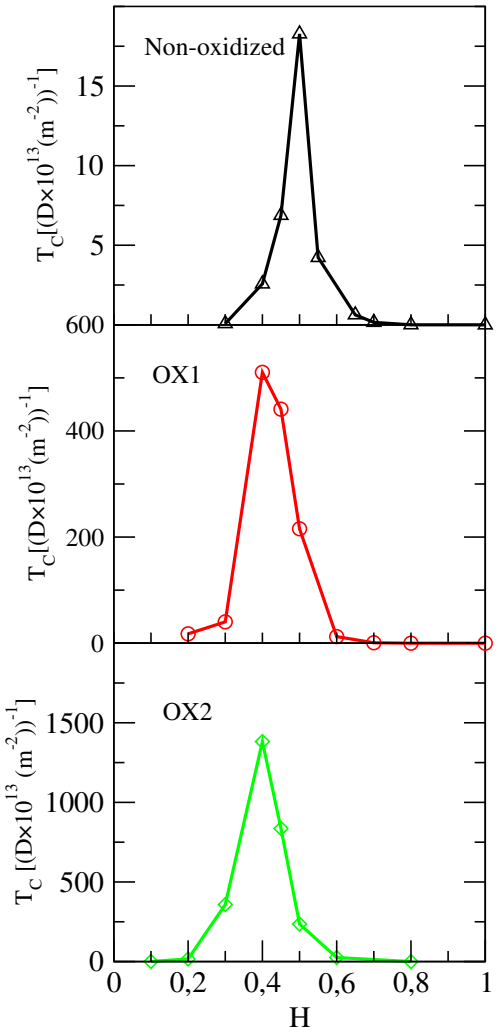

Figure 4.9: Frequency of translocations of NPs through non-oxidized bilayer (upper panel, data are obtained from Chapter3), oxidized bilayers OX1 (middle panel) and OX2 (down panel), calculated from Kramers theory, as a function of hydrophobicity.

peak of translocation rate is also observed at the critical hydrophobicity. Compared with the non-oxidized bilayer, a significant increase of the translocation rate of NPs is observed.

Oxidized Lipid Membrane Perturbation and Solvent Permeation Induced by NPs

The analysis addressed here is to clarify how membrane perturbation of the oxidized bilayers OX1 and OX2, induced by 50 and 100 NPs, changes upon oxidation. The results of membrane permeability for solvent of the oxidized bilayers OX1 and OX2, in the presence of 50 and 100 NPs of various hydrophobicity, are scaled with the results in the absence of NPs, respectively. For the oxidized bilayers, a considerable enhancement of membrane permeability is induced by NPs of hydrophobicity between $H = 0.4$ and $H = 0.8$. For the oxidized lipid bilayers, hydrophobic NPs with $H = 1$ can still affect the membrane permeability, contrary to the case of $H = 0$. A correlation between the membrane permeability for solvent and the area per lipid remains valid for the oxidized bilayers.

We characterize the membrane perturbation by the order parameter P_2 (Eq.1.1) as a function of the NPs' hydrophobicity. A minimum in the orientation order parameter around the critical hydrophobicity is displayed in the lower panel of Figure4.10, indicating a maximum membrane perturbation induced by the uptake of NPs. In terms of the membrane perturbation and membrane permeability for solvent induced by NPs, the oxidized bilayers OX1 and OX2 display a behavior that is similar to the non-oxidized bilayer.

4.4 Summary

In this Chapter, we presented a study of oxidized lipid bilayers and their interaction with NPs of various degrees of hydrophobicity. Two types of oxidized lipid molecules are considered in this study: introducing oxidation process on one tail or two tails. Changes of the structural and elastic properties of the bilayers upon oxidation have been examined on molecular level. Note that the oxidation reaction induced by the addition of the hydrophilic polar beads in the tails leads to an expansion of the surface area, accompanied with the decrease of membrane thickness and a dramatic drop of the stretching modulus. The membrane permeability for solvent increases significantly upon oxidation. These phenomena observed are related to the oxidation effect.

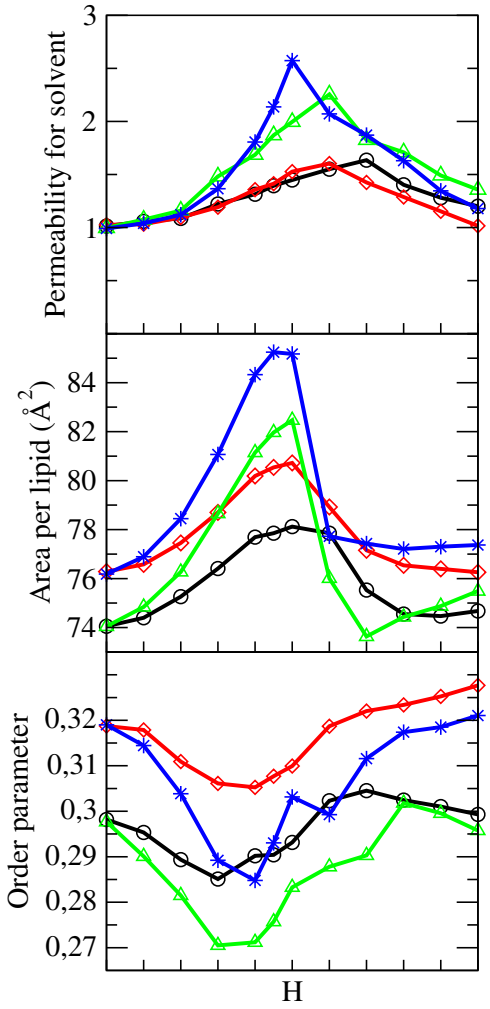

Figure 4.10: The membrane permeability for solvent (upper panel), the area per lipid (middle panel), and the order parameter of lipid tails (lower panel) as a function of hydrophobicity H, in the presence of 50 and 100 NPs, respectively. Here, black lines (circles) and green lines (triangles) denote the results for the oxidized bilayer OX1 interacting with 50 and 100 NPs, respectively. Red lines (diamonds) and blue lines (stars) present the results for the oxidized bilayer OX2 interacting with 50 and 100 NPs, respectively.

The interactions between the oxidized bilayer and NPs of various degrees of hydrophobicity have been further studied. In Chapter3and in Ref. [111], the potential model for the non-oxidized bilayer is confirmed, and high translocation rates at the critical hydrophobicity are observed. The results for the oxidized lipid bilayers are consistent with previous findings: the potential model remains valid. Moreover, the translocation rate of NPs at critical hydrophobicity increases significantly compared to the case of non-oxidized bilayers. This result has been confirmed by the study of the free energy landscapes of NP translocation through bilayers, in which the presence of oxidized beads reduces the free energy barrier to about 5 k_BT and 3.5 k_BT, for the oxidized bilayers OX1 and OX2, respectively. These findings imply that the average hydrophobicity of the bilayers decreases upon oxidation and that the bilayers become softer upon oxidation. This could provide a new strategy for applications in drug delivery and membrane permeability by introducing the oxidation effect. For oxidized bilayers, the membrane perturbation and membrane permeability for solvent, induced by NPs, are consistent with the case of non-oxidized bilayer. These findings give insight into the NPs' toxicity to the oxidized bilayers.

5 Summary and Outlook

Self-organized amphiphilic membranes in the liquid state may be regarded either as potential traps or potential barriers with respect to NPs, depending on their hydrophobicity. Systematic studies of NP-membrane interactions are of great importance for bioapplications, especially for drug delivery. On the other hand, comprehensive investigations of membrane perturbation induced by the NPs can improve the understanding of the toxicity of NPs.

The role of the hydrophobicity of NPs in the translocation rate is examined by calculating the potential of mean force of the NPs. Both results regarding 50 and 100 NPs coincide, display a narrow window of high translocation rates for NPs with a balanced hydrophobicity close to $H = 0.5$, thus verify the potential model of the lipid membrane. At this point, the free energy landscape is maximally flat and the remaining barrier can be associated with the entropy reduction of the tails while accommodating the NPs. The latter is only of the order of a few k_BT, which explains the high translocation rates. Using Kramers theory, the passive translocation of NPs, as observed in the simulations, can be related with the mean first-passage time of a diffusing particle in the free energy profile. When the concentration of NPs is sufficiently high, cooperative effects are observed. This can be verified by the notable flatter free energy barrier for translocation with increasing number of NPs. Particularly, due to the inhomogeneous distribution inside the membrane, collective effects play an important role in different kinetic pathways of translocation of NPs with intermediate hydrophobicities.

In order to relate the microscopic definition of hydrophobicity of NPs, which is based on the coarse-grained interaction model, a water/oil system is simulated and the free energy difference between water and oil phases for the NP is calculated. The results show a linear relation between our microscopic parameter H and the partition coefficient of the NP between the two phases. Based on these results, the hydrophobicity constant in the simulations can be quantified with an experimentally accessible partition coefficient.

The uptake of NPs changes the properties of the lipid bilayer. As observed in previous

studies, partially hydrophobic NPs, i.e. $0 < H < 1$, enhance the membrane permeability for water considerably. Our simulation results display a correlation between the area per lipid and the NP-induced permeability of the membrane. Note that these effects are not related to any pore formation of the membrane, but rather a consequence of the fact that a self-organized lipid layer in liquid state represents a free energy barrier/landscape for nano-objects.

To investigate the oxidation effect, further studies of oxidized lipid bilayers and their interactions with NPs of various degrees of hydrophobicity, are conducted. Two oxidatively modified lipids are considered by introducing a hydrophilic oxidized bead to either one tail or two tails. Due to the hydrophilic characteristic of oxidized beads, the lipid tails tend to bend towards the lipid head-tail interface. This conformation change leads to an expansion of the surface area, accompanied with the decrease of membrane thickness and the order parameter of the tail, as well as a dramatic drop of stretching modulus. The study of the interactions between oxidized bilayers and NPs shows that for oxidized bilayers the critical hydrophobicity corresponding to the maximal translocation rate of NPs, shifts towards the hydrophilic region. This finding is related to the decrease of average hydrophobicity in the core of the oxidized bilayer. Additionally, the translocation rate of NPs at critical hydrophobicity increases significantly, compared to the case of non-oxidized bilayers. This is consistent with a reduction of the free energy barrier of the oxidized lipid bilayer. This phenomenon can be further exploited as a new strategy for an application in drug delivery and controlling the membrane permeability through the oxidation effect.

Bibliography

(1) Iwai, I.; Han, H.; Den Hollander, L.; Svensson, S.; Oefverstedt, L.-G.; Anwar, J.; Brewer, J.; Bloksgaard, M.; Laloeuf, A.; Nosek, D., et al. *J. Invest. Dermatol.* **2012**, *132*, 2215–2225.

(2) Briganti, S.; Picardo, M. *J. Eur. Acad. Dermatol. Venereol.* **2003**, *17*, 663–669.

(3) Mouritsen, O. G.; Jørgensen, K. *Pharm. Res.* **1998**, *15*, 1507–1519.

(4) Fahr, A.; van Hoogevest, P.; May, S.; Bergstrand, N.; Leigh, M. L. *Eur. J. Pharm. Sci.* **2005**, *26*, 251–265.

(5) Besterman, J. M.; Low, R. B. *Biochem. J.* **1983**, *210*, 1.

(6) Battey, N. H.; James, N. C.; Greenland, A. J.; Brownlee, C. *The Plant Cell* **1999**, *11*, 643–659.

(7) Cullis, P. t.; De Kruijff, B. *BBA -Rev. Biomembranes* **1979**, *559*, 399–420.

(8) Gorter, E.; Grendel, F. *J. Exp. Med.* **1925**, *41*, 439–443.

(9) Singer, S. J.; Nicolson, G. L. *Science* **1972**, *175*, 720–731.

(10) Venturoli, M.; Sperotto, M. M.; Kranenburg, M.; Smit, B. *Phys. Rep.* **2006**, *437*, 1–54.

(11) Borst, J. W.; Visser, N. V.; Kouptsova, O.; Visser, A. J. *BBA-Mol. Cell Biol. Lipids* **2000**, *1487*, 61–73.

(12) Suda, Y.; Tero, R.; Yamashita, R.; Yusa, K.; Takikawa, H. *Jpn. J. Appl. Phys.* **2016**, *55*, 03DF05.

(13) Megli, F. M.; Russo, L.; Sabatini, K. *FEBS letters* **2005**, *579*, 4577–4584.

(14) Megli, F. M.; Sabatini, K. *FEBS letters* **2003**, *550*, 185–189.

(15) Megli, F. M.; Sabatini, K. *FEBS letters* **2004**, *573*, 68–72.

(16) Lis, M.; Wizert, A.; Przybylo, M.; Langner, M.; Swiatek, J.; Jungwirth, P.; Cwiklik, L. *Phys. Chem. Chem. Phys.* **2011**, *13*, 17555–17563.

(17) Wong-Ekkabut, J.; Xu, Z.; Triampo, W.; Tang, I.-M.; Tieleman, D. P.; Monticelli, L. *Biophys. J.* **2007**, *93*, 4225–4236.

(18) Berman, S. B.; Hastings, T. G. *J. Neurochem.* **1999**, *73*, 1127–1137.

(19) Yusupov, M.; Van der Paal, J.; Neyts, E.; Bogaerts, A. *BBA-Gen. Subjects* **2017**, *1861*, 839–847.

(20) Leonarduzzi, G.; Arkan, M. C.; Başağa, H.; Chiarpotto, E.; Sevanian, A.; Poli, G. *Free Rad. Biol. Med.* **2000**, *28*, 1370–1378.

(21) Zima, T.; Kalousova, M. *Alcohol Clin. Exp. Res.* **2005**, *29*.

(22) Halliwell, B.; Gutteridge, J. M. *Methods Enzymol.* **1990**, *186*, 1–85.

(23) Deigner, H.-P.; Hermetter, A. *Curr. Opin. Lipidol.* **2008**, *19*, 289–294.

(24) Everse, J.; Coates, P. W. *Free Rad. Bio. Med.* **2005**, *38*, 1296–1310.

(25) Dexter, D.; Carter, C.; Wells, F.; Javoy-Agid, F.; Agid, Y.; Lees, A.; Jenner, P.; Marsden, C. D. *J. Neurochem.* **1989**, *52*, 381–389.

(26) Butterfield, D. A.; Drake, J.; Pocernich, C.; Castegna, A. *Trends Mol. Med.* **2001**, *7*, 548–554.

(27) Nagle, J. F.; Zhang, R.; Tristram-Nagle, S.; Sun, W.; Petrache, H. I.; Suter, R. M. *Biophys. J.* **1996**, *70*, 1419–1431.

(28) Seelig, J.; Seelig, A. *Q. Rev. Biophys.* **1980**, *13*, 19–61.

(29) Heyn, M. P. *FEBS letters* **1979**, *108*, 359–364.

(30) Nagle, J. F.; Tristram-Nagle, S. *BBA-Rev. Biomembranes* **2000**, *1469*, 159–195.

(31) McIntosh, T.; Simon, S. *Biochemistry* **1986**, *25*, 4948–4952.

(32) Nagle, J. *Biophys. J.* **1993**, *64*, 1476–1481.

(33) Müller, M.; Katsov, K.; Schick, M. *Phys. Rep.* **2006**, *434*, 113–176.

(34) Deserno, M.; Kremer, K.; Paulsen, H.; Peter, C.; Schmid, F. In *From single molecules to nanoscopically structured materials*; Springer: 2013, pp 237–283.

(35) Brooks, B. R.; Bruccoleri, R. E.; Olafson, B. D.; States, D. J.; Swaminathan, S. a.; Karplus, M. *J. Comput. Chem.* **1983**, *4*, 187–217.

(36) Van Gunsteren, W. F.; Billeter, S. R.; Eising, A. A.; Hünenberger, P. H.; Krüger, P.; Mark, A. E.; Scott, W. R.; Tironi, I. G. **1996**.

(37) Marrink, S. J.; De Vries, A. H.; Mark, A. E. *J. Phys. Chem. B* **2004**, *108*, 750–760.

(38) Marrink, S. J.; Risselada, H. J.; Yefimov, S.; Tieleman, D. P.; De Vries, A. H. *J. Phys. Chem. B* **2007**, *111*, 7812–7824.

(39) Monticelli, L.; Kandasamy, S. K.; Periole, X.; Larson, R. G.; Tieleman, D. P.; Marrink, S.-J. *J. Chem. Theory Comput.* **2008**, *4*, 819–834.

(40) Uusitalo, J. J.; Inglfsson, H. I.; Akhshi, P.; Tieleman, D. P.; Marrink, S. J. *J. Chem. Theory. Comput.* **2015**, *11*, 3932–3945.

(41) López, C. A.; Rzepiela, A. J.; De Vries, A. H.; Dijkhuizen, L.; Hnenberger, P. H.; Marrink, S. J. *J. Chem. Theory Comput.* **2009**, *5*, 3195–3210.

(42)Cooke, I. R.; Deserno, M. *Biophys. J.* **2006**, *91*, 487–495.
(43) Schmid, F.; Düchs, D.; Lenz, O.; West, B. *Comput. Phys. Commun.* **2007**, *177*, 168–171.
(44)Düchs, D.; Schmid, F. *J. Phys.: Condens. Matter* **2001**, *13*, 4853.
(45)Lenz, O.; Schmid, F. *Phys. Rev. Lett.* **2007**, *98*, 058104.
(46) Sommer, J.-U.; Werner, M.; Baulin, V. A. *EPL (Europhysics Letters)* **2012**, *98*, 18003.
(47)Werner, M.; Sommer, J.-U.; Baulin, V. A. *Soft Matter* **2012**, *8*, 11714–11722.
(48)Werner, M.; Sommer, J.-U. *Biomacromolecules* **2014**, *16*, 125–135.
(49)Rabbel, H.; Werner, M.; Sommer, J.-U. *Macromolecules* **2015**, *48*, 4724–4732.
(50)Checkervarty, A.; Werner, M.; Sommer, J.-U. *Soft Matter* **2018**.
(51) Pogodin, S.; Werner, M.; Sommer, J.-U.; Baulin, V. A. *Acs Nano* **2012**, *6*, 10555–10561.
(52)Ginzburg, V. V.; Balijepalli, S. *Nano Lett.* **2007**, *7*, 3716–3722.
(53) Roiter, Y.; Ornatska, M.; Rammohan, A. R.; Balakrishnan, J.; Heine, D. R.; Minko, S. *Nano Lett.* **2008**, *8*, 941–944.
(54)Lewinski, N.; Colvin, V.; Drezek, R. *Small* **2008**, *4*, 26–49.
(55) Pan, Y.; Neuss, S.; Leifert, A.; Fischler, M.; Wen, F.; Simon, U.; Schmid, G.; Brandau, W.; Jahnen-Dechent, W. *Small* **2007**, *3*, 1941–1949.
(56) Connor, E.; Mwamuka, J.; Gole, A.; Murphy, C.; Wyatt, M. *Small* **2005**, *1*, 325–327.
(57) Gelperina, S.; Kisich, K.; Iseman, M. D.; Heifets, L. *Am. J. Respir. Crit. Care Med.* **2005**, *172*, 1487–1490.
(58)Cho, K.; Wang, X.; Nie, S.; Shin, D. M. *Clin. Cancer Res.* **2008**, *14*, 1310–1316.
(59) Wang, B.; Zhang, L.; Bae, S. C.; Granick, S. *Proc. Natl. Acad. Sci. USA* **2008**, *105*, 18171–18175.
(60) Leroueil, P. R.; Berry, S. A.; Duthie, K.; Han, G.; Rotello, V. M.; McNerny, D. Q.; Baker, J. R.; Orr, B. G.; Banaszak Holl, M. M. *Nano Lett.* **2008**, *8*, 420–424.
(61)Lin, J.; Zhang, H.; Chen, Z.; Zheng, Y. *ACS nano* **2010**, *4*, 5421–5429.
(62)Chithrani, D. B.; Ghazani, A. A.; Chan, W. C. *Nano Lett.* **2006**, *6*, 662–668.
(63)Chithrani, D. B.; Chan, W. C. *Nano Lett.* **2007**, *7*, 1542–1550.
(64) Jiang, W.; Kim, B. Y.; Rutka, J. T.; Chan, W. C. *Nat. Nanotechnol.* **2008**, *3*, 145–150.
(65) Lin, I.-C.; Liang, M.; Liu, T.-Y.; Ziora, Z. M.; Monteiro, M. J.; Toth, I. *Biomacromolecules* **2011**, *12*, 1339–1348.
(66)Lin, X.; Li, Y.; Gu, N. *J. Comput. Theor. Nanosci.* **2010**, *7*, 269–276.

(67)Gupta, R.; Rai, B. *J. Phys. Chem. B* **2016**, *120*, 7133–7142.
(68)Dasgupta, S.; Auth, T.; Gompper, G. *Nano Lett.* **2014**, *14*, 687–693.
(69)Yang, K.; Ma, Y.-Q. *Nat. Nanotechnol.* **2010**, *5*, 579–583.
(70)Bloom, M.; Evans, E.; Mouritsen, O. G. *Q. Rev. Biophys.* **1991**, *24*, 293–397.
(71) Allen, M. P.; Tildesley, D. J., *Computer simulation of liquids*; Oxford university press: 2017.
(72) Haile, J.; Johnston, I.; Mallinckrodt, A. J.; McKay, S., et al. *Comput. in Phys.* **1993**, *7*, 625–625.
(73)Kjellander, R.; Marčelja, S. *Chem. Phys. Lett.* **1985**, *120*, 393–396.
(74)Van der Ploeg, P.; Berendsen, H. *J. Chem. Phys.* **1982**, *76*, 3271–3276.
(75) Rapaport, D. C.; Blumberg, R. L.; McKay, S. R.; Christian, W., et al. *Computers in Physics* **1996**, *10*, 456–456.
(76) Butcher, J. C., *Numerical methods for ordinary differential equations*; John Wiley & Sons: 2016.
(77) Swope, W. C.; Andersen, H. C.; Berens, P. H.; Wilson, K. R. *J. Chem. Phys.* **1982**, *76*, 637–649.
(78) Hockney, R. W.; Eastwood, J. W., *Computer simulation using particles*; crc Press: 1988.
(79)Ewald, P. P. *Ann. Phys* **1921**, *64*, 253–287.
(80) Berendsen, H. J.; Postma, J. v.; van Gunsteren, W. F.; DiNola, A.; Haak, J. *J. Chem. Phys.* **1984**, *81*, 3684–3690.
(81)Andersen, H. C. *J. Chem. Phys.* **1980**, *72*, 2384–2393.
(82)Hoover, W. G. *Phys. Rev. A* **1986**, *34*, 2499.
(83) Martyna, G. J.; Tobias, D. J.; Klein, M. L. *J. Chem. Phys.* **1994**, *101*, 4177–4189.
(84)Schneider, T.; Stoll, E. *Phys. Rev. B* **1978**, *17*, 1302.
(85) Rogge, S.; Vanduyfhuys, L.; Ghysels, A.; Waroquier, M.; Verstraelen, T.; Maurin, G.; Van Speybroeck, V. *J. Chem. Theory Comput.* **2015**, *11*, 5583–5597.
(86) Frenkel, D.; Smit, B., *Understanding molecular simulation: from algorithms to applications*; Academic press: 2001; Vol. 1.
(87) Berendsen, H. J., *Simulating the physical world: hierarchical modeling from quantum mechanics to fluid dynamics*; Cambridge University Press: 2007.
(88)Torrie, G. M.; Valleau, J. P. *Chem. Phys. Lett.* **1974**, *28*, 578–581.
(89)Torrie, G. M.; Valleau, J. P. *J. Comput. Phys.* **1977**, *23*, 187–199.
(90)McDonald, I.; Singer, K. *J. Chem. Phys.* **1967**, *47*, 4766–4772.
(91)McDonald, I.; Singer, K. *J. Chem. Phys.* **1969**, *50*, 2308–2315.

(92)Kästner, J. *WIREs: Comput. Mol. Sci.* **2011**, *1*, 932–942.
(93)Ferrenberg, A. M.; Swendsen, R. H. *Phys. Rev. Lett.* **1989**, *63*, 1195.
(94) Kumar, S.; Rosenberg, J. M.; Bouzida, D.; Swendsen, R. H.; Kollman, P. A. *J. Comput. Phys.* **1992**, *13*, 1011–1021.
(95)Souaille, M.; Roux, B. *Comput. Phys. Commun.* **2001**, *135*, 40–57.
(96) Aymonier, C.; Schlotterbeck, U.; Antonietti, L.; Zacharias, P.; Thomann, R.; Tiller, J. C.; Mecking, S. *Chem. Commun.* **2002**, 3018–3019.
(97) Tkachenko, A. G.; Xie, H.; Coleman, D.; Glomm, W.; Ryan, J.; Anderson, M. F.; Franzen, S.; Feldheim, D. L. *J. Am. Chem. Soc.* **2003**, *125*, 4700–4701.
(98)Brigger, I.; Dubernet, C.; Couvreur, P. *Adv. Drug Deliv. Rev.* **2012**, *64*, 24–36.
(99) Chen, M.; Yamamuro, S.; Farrell, D.; Majetich, S. A. *J. Appl. Phys.* **2003**, *93*, 7551–7553.
(100) Moyano, D. F.; Goldsmith, M.; Solfiell, D. J.; Landesman-Milo, D.; Miranda, O. R.; Peer, D.; Rotello, V. M. *J. Am. Chem. Soc.* **2012**, *134*, 3965–3967.
(101) Lindman, S.; Lynch, I.; Thulin, E.; Nilsson, H.; Dawson, K. A.; Linse, S. *Nano lett.* **2007**, *7*, 914–920.
(102) Park, S.-H.; Oh, S.-G.; Mun, J.-Y.; Han, S.-S. *Colloids Surf. B: Biointerfaces* **2006**, *48*, 112–118.
(103) Park, S.-H.; Oh, S.-G.; Mun, J.-Y.; Han, S.-S. *Colloids Surf. B: Biointerfaces* **2005**, *44*, 117–122.
(104) Verma, A.; Uzun, O.; Hu, Y.; Hu, Y.; Han, H.-S.; Watson, N.; Chen, S.; Irvine, D. J.; Stellacci, F. *Nat. Mater.* **2008**, *7*, 588–595.
(105) Gkeka, P.; Sarkisov, L.; Angelikopoulos, P. *J. Phys. Chem. Lett.* **2013**, *4*, 1907–1912.
(106) Pogodin, S.; Werner, M.; Sommer, J.-U.; Baulin, V. A. *ACS nano* **2012**, *6*, 10555–10561.
(107)Sommer, J.-U.; Werner, M.; Baulin, V. A. *Europhys. Lett.* **2012**, *98*, 18003.
(108)Werner, M.; Sommer, J.-U.; Baulin, V. A. *Soft Matter* **2012**, *8*, 11714–11722.
(109)Werner, M.; Sommer, J.-U. *Biomacromolecules* **2014**, *16*, 125–135.
(110)Jing, B.; Zhu, Y. *J. Am. Chem. Soc.* **2011**, *133*, 10983–10989.
(111) Su, C.-F.; Merlitz, H.; Rabbel, H.; Sommer, J.-U. *J. Phys. Chem. Lett.* **2017**, *8*, 4069–4076.
(112)Carruthers, A.; Melchior, D. *Biochemistry* **1983**, *22*, 5797–5807.
(113)Andrasko, J.; Forsén, S. *Biochem. Biophys. Res. Commun.* **1974**, *60*, 813–819.
(114)Marrink, S.-J.; Berendsen, H. J. *J. Phys. Chem.* **1994**, *98*, 4155–4168.

(115)Plimpton, S. *J. Comput. Phys.* **1995**, *117*, 1–19.
(116)Schulz, M.; Olubummo, A.; Binder, W. H. *Soft Matter* **2012**, *8*, 4849–4864.
(117)Halperin, A.; Kroger, M.; Zhulina, E. *Macromolecules* **2011**, *44*, 3622–3638.
(118) Halperin, A.; Fragneto, G.; Schollier, A.; Sferrazza, M. *Langmuir* **2007**, *23*, 10603–10617.
(119)Halperin, A.; Kroger, M. *Langmuir* **2009**, *25*, 11621–11634.
(120)Merlitz, H.; Wu, C.-X.; Sommer, J.-U. *Macromolecules* **2012**, *45*, 8494–8501.
(121)Gardiner, C. *Springer Berlin* **1985**.
(122)Schulten, K.; Schulten, Z.; Szabo, A. *J. Chem. Phys.* **1981**, *74*, 4426–4432.
(123)Hänggi, P.; Talkner, P.; Borkovec, M. *Rev. Mod. Phys.* **1990**, *62*, 251.
(124)Shinoda, W. *BBA.-Biomembranes* **2016**, *1858*, 2254–2265.
(125)Radzicka, A.; Wolfenden, R. *Biochemistry* **1988**, *27*, 1664–1670.
(126)Wolfenden, R. *J. Gen. Physiol.* **2007**, *129*, 357–362.
(127) MacCallum, J. L.; Bennett, W. D.; Tieleman, D. P. *Biophys. J.* **2008**, *94*, 3393–3404.
(128)Reis, A.; Spickett, C. M. *BBA-Biomembranes* **2012**, *1818*, 2374–2387.
(129)Davies, M. J. *Biochem. J.* **2016**, *473*, 805–825.
(130) Halliwell, B.; Gutteridge, J. M., *Free radical in biology and medicine*; Oxford University Press, USA: 2015.
(131)Stratton, S. P.; Liebler, D. C. *Biochemistry* **1997**, *36*, 12911–12920.
(132) Cazzola, R.; Rondanelli, M.; Russo-Volpe, S.; Ferrari, E.; Cestaro, B. *J. Lipid Res.* **2004**, *45*, 1846–1851.
(133) Volinsky, R.; Cwiklik, L.; Jurkiewicz, P.; Hof, M.; Jungwirth, P.; Kinnunen, P. K. *Biophys. J.* **2011**, *101*, 1376–1384.
(134)Ray, P. D.; Huang, B.-W.; Tsuji, Y. *Cell. Signal.* **2012**, *24*, 981–990.
(135)Pelicano, H.; Carney, D.; Huang, P. *Drug Resist. Updates* **2004**, *7*, 97–110.
(136)Schumacker, P. T. *Cancer cell* **2006**, *10*, 175–176.
(137) Trachootham, D.; Alexandre, J.; Huang, P. *Nat. Rev. Drug Discov.* **2009**, *8*, 579–591.
(138) Kohanski, M. A.; Dwyer, D. J.; Hayete, B.; Lawrence, C. A.; Collins, J. J. *Cell* **2007**, *130*, 797–810.
(139)Guo, Y.; Baulin, V. A.; Thalmann, F. *Soft matter* **2016**, *12*, 263–271.
(140) Weber, G.; Charitat, T.; Baptista, M. S.; Uchoa, A. F.; Pavani, C.; Junqueira, H. C.; Guo, Y.; Baulin, V. A.; Itri, R.; Marques, C. M., et al. *Soft Matter* **2014**, *10*, 4241–4247.

(141) Aoki, P.; Schroder, A.; Constantino, C.; Marques, C. *Soft matter* **2015**, *11*, 5995–5998.

List of Figures

1.1 Sketch of the lipid (left panel) and assembled lipid bilayer (right panel). .2
1.2 Structures of formations assembled by the corresponding lipids with different molecular shapes. 3
1.3 Mosaic model of the membrane: lipid bilayers and proteins attached/embedded in the membrane, adopted from Ref. [10]. 3

2.1 Lennard-Jones potential. 12
2.2 Periodic boundary conditions in two-dimensions. 14
2.3 Bias potential applied in windows along the reaction coordinate (upper panel). Biased free energy, bias potential and unbiased free energy in the window $\xi = 26$ (middle panel). Global free energy composed of direct MD simulation result and unbiased free energy in each window (lower panel).22

3.1 Upper panel: Sketch of the MARTINI model and simplified MARTINI model for lipids. Here, Q^+ and Q^- represent the zwitterionic headgroup. And h, t, b, s denote head, tail, bridge monomers of lipids and solvent beads. Lower panel: Sketch of interaction sites. 27
3.2 Snapshots: Lipid membranes interacting with 50 NPs, at different values of the hydrophobicity ($H = 0, 0.5, 0.8, 1$). Solvent beads are not shown to improve visibility. The solid lines displayed for $H = 0.5$ indicate the thresholds for calculating translocation events. This figure is adopted from Ref. [111] 31
3.3 Density profiles of the various components of the lipid membrane, as well as the NPs at different degrees of hydrophobicity ($H = 0, 0.2, 0.5, 0.8, 1$). Tail groups (black), head groups (green), lipid molecules (blue), NPs (red) and the solvent beads (purple) are presented as functions of distance from the center plane of the membrane, z. This figure is adopted from Ref. [111] 32
3.4 Translocation rates of NPs as a function of hydrophobicity, in the presence of 50 (black curve, circle symbols) and 100 NPs (red curve, diamond symbols). Brown line with triangle symbols present the results calculated from Kramers theory. Note that T_c in the last plot is in the scale of diffusion coefficient of NP (D). This figure is adopted from Ref. [111] 34

3.5 Free energy landscapes for a given NP in the presence of 50 and 100 NPs with hydrophobicity H=0.5. Here black and red lines present the cases of 50 and 100 NPs respectively. 36
3.6 Translocation rate per NP as a function of the number of NPs in the simulation box. 37
3.7 Sketch of the kinetic pathways of NPs with H=0.5 (red) and H=0.8 (blue) based on the analysis of the free energy landscape. The states of NPs are indicated as: solvent, interface, and core, i.e. between leaflets. The arrows indicate the rate of the processes. 38
3.8 Free energy profiles as a function of the distance from the membrane centre, in the presence of 50 NPs, and at different hydrophobicities, H. The reaction coordinate denotes the distance of the NP from the center of mass-plane of the membrane. The lipid head-tail interface is indicated by the orange dash lines. 40
3.9 Free energy profiles of NPs as a function of the distance from the center of the oil phase. The location of the interface between the water and the oil phases is indicated as a dashed vertical line. Here, black, blue, green, red, yellow, brown lines denote $H = 0, 0.3, 0.45, 0.5, 0.7, 1$. 42
3.10 Hydrophobicity scale: Free energy difference between water and oil phases for NPs as a function of hydrophobicity H. 43
3.11 Relative membrane permeability for solvent (upper panel), area per lipid (center panel), and order parameter of lipid tails (lower panel), as a function of the hydrophobicity H, and in the presence of 50 (black curves, open circle) and 100 (red curves, open diamond) NPs. 46

4.1 Scheme of the coarse-grained models for non-oxidized lipid, oxidized lipid oxidized with one tail and two tails. Here, h, t, O, o represent the lipid head, tail, hydrophobic and hydrophilic oxidized beads. 53
4.2 Comparisons of properties of non-oxidized bilayers as obtained in Chapter3and oxidized bilayers as obtained in the present chapter. 55
4.3 Density profiles of different species of non-oxidized bilayer (upper panel), lipid membranes oxidized with one tail (middle panel: OX1) and both tails (lower panel: OX2). Head group (red lines), tail group (black lines), hydrophobic oxidized group (blue lines), hydrophilic oxidized group (green lines), total density of lipid molecules (magenta lines) are presented as a function of distance from the center plane of the membrane, z. 57
4.4 The distribution of tilting angles of lipids for the non-oxidized bilayer (black line), the oxidized bilayers OX1 (red line) and OX2 (green line). 58
4.5 Hydrophobicity profiles of the non-oxidized bilayer (black line), oxidized bilayers OX1 (red line) and OX2 (green solid line). Here, the green dashed line denotes the average hydrophobicity of the core of the oxidized bilayer OX2. The core region is defined as the region between $z = z_{center} \pm 10$ Å, with z_{center} being the center of mass of the lipid membrane. 58

4.6 Density profiles of different species of oxidized bilayers OX1 (upper panel) and OX2 (lower panel) in the presence of 50 NPs of different hydrophobicity. Head group (black/dashed lines), tail group (magenta/dashed lines), hydrophobic oxidized group (blue/dashed lines), hydrophilic oxidized group (green/solid lines) and NPs (red/solid lines) are presented as a function of distance from the central plane of the membrane, z. The four different plots in the figure correspond to different levels of hydrophobicity, as indicated inside the plots. 60
4.7 Frequency of translocations of NPs through non-oxidized bilayer (upper panel), oxidized bilayers OX1 (middle panel) and OX2 (lower panel) as a function of hydrophobicity, in the presence of 50 and 100 NPs. Here, solid lines and dash lines denote the cases of 50 and 100 NPs, respectively. 62
4.8 The free energy profiles for NPs of different hydrophobicities translocation through the oxidized lipid membrane OX1 (left panel) and OX2 (right panel). Here, the lipid bilayer is perpendicular to the z coordinate. 63
4.9 Frequency of translocations of NPs through non-oxidized bilayer (upper panel, data are obtained from Chapter3), oxidized bilayers OX1 (middle panel) and OX2 (down panel), calculated from Kramers theory, as a function of hydrophobicity. 64
4.10 The membrane permeability for solvent (upper panel), the area per lipid (middle panel), and the order parameter of lipid tails (lower panel) as a function of hydrophobicity H, in the presence of 50 and 100 NPs, respectively. Here, black lines (circles) and green lines (triangles) denote the results for the oxidized bilayer OX1 interacting with 50 and 100 NPs, respectively. Red lines (diamonds) and blue lines (stars) present the results for the oxidized bilayer OX2 interacting with 50 and 100 NPs, respectively. 66

List of Tables

3.1 Characteristics of lipid bilayers constructed by original MARTINI model and simplified MARTINI model. 28

Erklärung

Hiermit versichere ich, dass ich die vorliegende Arbeit ohne unzulässige Hilfe Dritter und ohne Benutzung anderer als der angegebenen Hilfsmittel angefertigt habe; die aus fremden Quellen direkt oder indirekt übernommenen Gedanken sind als solche kenntlich gemacht. Die Arbeit wurde bisher weder im Inland noch im Ausland in gleicher oder ähnlicher Form einer anderen Prüfungsbehörde vorgelegt.

Die Arbeit wurde angefertigt unter Betreuung von Prof. Dr. Jens-Uwe Sommer am Leibniz-Institut für Polymerforschung Dresden e.V., Hohe Straße 6, 01069 Dresden.

Es haben betreffend meiner Person keine früheren erfolglosen Promotionsverfahren stattgefunden.

Weiter erkläre ich hiermit, dass ich die Promotionsordnung vom 23.02.2011 der Fakultät Mathematik und Naturwissenschaften der Technischen Universität Dresden anerkenne.

Chanfei Su, Dresden 06.06.2018